In-situ investigation of plasticity in a Ti-Al-V-Fe (#+#) alloy: Slip mechanisms, strain localization, and partitioning

In-situ investigation of plasticity in a Ti-Al-V-Fe (α+β) alloy: Slip mechanisms, strain localization, and partitioning

Shaolou Wei, Jinwoo Kim, and Cemal Cem Tasan*

Department of Materials Science and Engineering, Massachusetts Institute of Technology, Cambridge, MA02139, U.S.A.

Corresponding author: tasan@mit.edu (Cemal Cem Tasan)

Abstract: As one of the representative characteristics of plastic deformation, microstructural plastic strain inhomogeneity has triggered a broad interest in uncovering the corresponding deformation micro-mechanisms. (α+β) titanium alloys enable fruitful mechanistic explorations of this dependency, since: (i) the plastic anisotropy of the α-phase drives distinctive dislocation gliding and/or mechanical twinning modes for plastic strain accommodation; and (ii) deformation transferability between α/β phase boundaries strongly relies on both microstructural and structural parameters. The present work carried out in a Ti-Al-V-Fe (α+β) alloy is an in-situ mechanistic study, aiming to elucidate the critical deformation micro-mechanisms that are responsible for strain localization, partitioning, as well as damage inception processes. It is revealed through statistical analysis of the in-situ strain mapping results that a moderate partitioning trend exists between α- and β-phases, and that the present alloy is characterized by the eminent strain localization bands that develop at the early stage of plastic straining. Deformation micro-mechanisms including texture-facilitated prismatic $\langle \mathbf{a} \rangle$ slip activation together with the near-ideal slip transfer conditions across the α/β phase boundaries are found to be predominant in the strain localization region. The combination of postmortem and in-situ damage analyses confirm the dominant role of these long-range strain localization bands in expediting surface cracking events.

Keywords: A. microstructures; B. polycrystalline material, metallic material; C. electron microscopy.

1. Introduction

Heterogeneous deformation in polycrystalline metallic materials is of fundamental significance in bridging deformation micro-mechanisms and macroscopic load-bearing response (Bieler et al., 2009; Birosca et al., 2014; Charpagne et al., 2020; Yang et al., 2011). Grain boundaries (GBs) and phase boundaries (PBs), have been well-documented to actively govern local stress and strain distribution evolutions, and thereby the strain localization and damage behavior (Bieler et al., 2014; Gurtin, 2008; Sperry et al., 2020; Wei et al., 2019b; Z. Zhang et al., 2018) The role of GBs have been widely discussed with regards to crystallographic orientation effects (Bayerschen et al., 2016; Hall E. O., 1951; Hémery et al., 2018; Li et al., 2019), which create inhomogeneity even within the volumes of individual grains due to the spatially-varying deformation rates therein (Stinville et al., 2016). In addition to these classical Hall-Petch-like concepts, more recent crystal plasticity investigations also highlight the role of local strain energy in accurately correlating GB-induced heterogeneous deformation with damage incipience (Chen et al., 2018; Cruzado et al., 2018; Musinski and McDowell, 2016). Unlike the appreciable exploration of

plastic deformation considering GBs, relevant research towards PBs remains limited. Extra complexities involved with PBs are mainly two fold: chemically, diffusional phase transformation pathways inevitably introduce elemental partitioning, which hinders accurate modelling of PB structures at the atomistic level (Bormann et al., 2019; Takahashi et al., 2017); and mechanically, distinctive crystallographic structure as well as mechanical property differences amongst presenting phases complicates the establishment of concisely reliable constitutive laws (Fan et al., 2018; Kapoor et al., 2018). Recent advancement of microstructure-based strain mapping (μ-DIC) approaches as well as crystal plasticity simulations have resolved the foregoing challenges to some extent (Cappola et al., 2021; Roters et al., 2010; Stinville et al., 2021; Yan et al., 2015). One exemplary accomplishment is the progress in dual-phase steels investigations (Khosravani et al., 2017; Tasan et al., 2015; Yongsheng Xu et al., 2020), where the ferrite/martensite PBs are recognized to retard deformation transfer and the resultant interfacial strain incompatibility is predominant throughout the whole plastic realm (Das et al., 2019; Han et al., 2014; Kuang et al., 2009). It would be therefore expected that the PB-induced heterogeneous deformation can appear more intriguing once comparable deformability present in existing phases. In light of this, two-phase titanium alloys provide an effective platform to closely examine the correlation between PB-related deformation micro-mechanisms and the evolution of heterogeneous deformation at the meso-scale.

As two-phase titanium alloys consist of hexagonal close packed (HCP)-structured α-phase (major constituent) and body centered cubic (BCC) structured β-phase (minor constituent), plastic deformation features have great diversity in both structural and microstructural aspects (Banerjee and Williams, 2013; Semiatin, 2020). In contrast to the higher symmetry face-centered cubic (FCC) structure, the HCP lattice reveals intrinsic plastic anisotropy (Ahmad et al., 2020; Joseph et al., 2018; Yoo, 1981). Compatible plastic flow in HCP structures, as dictated by the von Mises criterion (Anderson et al., 2017), generally requires five independent active slip systems. However, the activation of both basal $\langle \mathbf{a} \rangle$ and prismatic $\langle \mathbf{a} \rangle$ slip, which are apparently the two slip modes with the lowest critical resolved shear stress (CRSS) magnitudes, can only contribute to four independent slip systems. This signifies the necessity of activating additional deformation micro-events especially to accommodate plastic strain along the $\langle \mathbf{c} \rangle$ axis. As such, mechanistic studies of pyramidal $\langle \mathbf{c}+\mathbf{a} \rangle$ slip, extension and/or contraction twinning modes in α-Ti have highlighted their fundamental contributions to the macroscopic mechanical response (Nervo et al., 2016; Proust et al., 2007; Wei et al., 2021; Zhou et al., 2019). The β-phase, on the other hand, has less pronounced plastic anisotropy, in which $\{110\}\langle 1\bar{1}1\rangle$, $\{112\}\langle 11\bar{1}\rangle$, and $\{123\}\langle 11\bar{1}\rangle$ dislocation slip modes are well-documented as the major deformation micro-mechanisms. Although systematic experimental data on the dependency of alloying elements on the CRSS magnitudes of β-phase is rather lacking, exemplary studies on commercial (α+β) Ti6242 (Deka et al., 2006; Venkatramani et al., 2007; Zhang et al., 2016) and Ti64 (Stapleton et al., 2008; Warwick et al., 2012a) alloys consistently reveal similar CRSS magnitudes between potential slip modes in the β-phase and prismatic $\langle \mathbf{a} \rangle$ slip in the α-phase. Such intrinsically moderate slip strength contrast renders cooperative deformation between α- and β-phases, which reveals deformation transferability across α/β PBs motivated in this investigation.

Early transmission electron microscopy (TEM) studies on Ti6242 and Ti64 alloys led to the conclusion that slip transfer across α/β PBs most commonly takes place, in cases where there are Burgers vectors with similar lengths and directions on both sides of the PBs (Savage et al., 2004; Suri et al., 1999). Recent meso-scale experimental studies based on integrating electron backscatter diffraction (EBSD) approach, micro-pillar compression, and crystallographic calculations also reflect the Burgers orientation relation (BOR) on slip transferability across α/β PBs (He et al., 2014; Jun et al., 2019; Seal et al., 2012; Zhang et al., 2016). In addition to these experimental efforts, the quick emergence of multi-scale simulation methods has enabled the exploration of such a deformation micro-event in greater depth. By incorporating density functional theory (DFT) to the microscopic phase field framework, the generalized stacking fault energy was recently established for α/β PB slip transfer in a Ti6242 alloy (Zhao et al., 2019). The involvement of Shockley partials was identified as the critical atomistic mechanism that facilitates slip transfer and hence alleviates geometrically necessary dislocation nucleation. Coupled discrete dislocation dynamics (DDD) and crystal plasticity finite element methods (CPFEM) simulation, on the other hand, has elucidated how local stress and/or strain distribution contributes to individual slip transfer events in micro-pillar compression experiments (Waheed et al., 2019; Yilun Xu et al., 2020; Zheng et al., 2018, 2017a).

Depending on alloying elements and thermomechanical processing history, (α+β) titanium alloys can exhibit a broad spectrum of microstructures, spanning from Widmanstatten lamellae, basketweave, and equiaxed morphology (Cui et al., 2021; Gil et al., 2001; Kim et al., 2008; Wei et al., 2021, 2016; Wu et al., 2021). Especially at ambient temperature, the equiaxed microstructure exhibits a more desirable strength-ductility combination (Banerjee and Williams, 2013; Peters and Leyens, 2003). In fact, one of the prototypical concepts of achieving equiaxed microstructure in (α+β) alloys is to reduce the slip length down to the scale of α-grain size, such that the inferior slip resistance in the retained β-layer, which is along the α-grain boundaries, can be mitigated (Castany et al., 2008; Peters and Leyens, 2003; Wang et al., 2020). However, in-situ experimental studies have revealed that the validity of this sort of microstructure design approach largely depends on the crystallographic texture of the α-phase. Exemplary in-situ studies on equiaxed Ti64 alloys proved that the sub-millimeter microstructure regions can discernibly increase the slip length via the similar slip mode activation propensity together with the smooth slip transferability across low-angle GBs in the α-phase (H émery et al., 2019; Kasemer et al., 2017). The magnified slip length, as a result, leads to inception of extensive strain localization bands, expediting surface crack nucleation, which is harmful to macroscopic load-bearing performances (Cappola et al., 2021). Under these circumstances, the presence of geometrically non-negligible β-phase (such as near-equiaxed β-phase) will in turn further complicate the deformation micro-features. A recent study performed on an equiaxed Ti-1.0 Fe wt.% (α+β) alloy revealed the apparent strain partitioning trend resulting from the higher hardness of the β-phase (Chong et al., 2020), which proved to be the dominant factor for phase boundary micro-cracking.

The present study employs a Ti-Al-V-Fe (α+β) alloy with a rolling texture, aiming to explore the following three fundamental

topics: (1) what deformation micro-events are associated with strain localization band development and its propagation? (2) how is plastic strain accommodated by the α- and β- phases? and (3) how do the micro-events and/or mechanisms identified in (1) and (2) influence the micro-damage and thereby macroscopic failure procedure? By carrying out in-situ experiments and crystallographic calculations, we reveal that: (1) the strain localization region is mostly characterized by predominant prismatic ⟨**a**⟩ slip activation, and the near-ideal slip transferability across the α/β PBs; (2) plastic strain partitioning appears generally moderate between α- and β-phases; and (3) coupled post-mortem and in-situ damage mechanism studies confirm that strain localization bands are mostly accounting for the development of surface crack while the major failure mechanisms in the bulk is the nucleation and growth of micro-voids.

2. Material and methods

2.1 Microstructural characterization and ex-situ mechanical property assessment

The material investigated in the present study is a fully-recrystallized Ti-4.0Al-2.5V-1.5Fe wt. % (α+β) alloy (Fig. 1) supplied by Allegheny Technologies Incorporated (ATI), Natrona Heights, PA, USA. Microstructural characterizations including secondary electron (SE), back scatter electron (BSE) imaging, energy-dispersive X-ray spectroscopy (EDS, EDAX Octane Elite Plus detector), and EBSD (EDAX Hikari camera, 18.00 mm working distance under 20 kV acceleration voltage) were carried out in a TSCAN MIRA 3 scanning electron microscope (SEM). An Orientation Imaging Microscopy software (OIM, version 8.0) was employed to post-process the acquired EBSD patterns and to obtain crystallographic information for theoretical calculations. Rectangular dog bone-shaped tensile specimens (gauge dimension: 6.5×2.5×1.0 mm^3) were sectioned along the rolling direction (RD) of the bulk alloy sheet using electrical discharge machining (EDM). These specimens were then subjected to mechanical grinding up to #1200 SiC abrasive paper before being speckle patterned for optical digital image correlation (DIC) measurement. Ex-situ uniaxial tensile testing was performed on a Gatan micro-mechanical testing platform under a quasi-static loading condition (strain rate: 10^{-3} s^{-1}), during which optical images were recorded every 1 s for strain profile assessment in a GOM software (https://www.gom.com/3d-software/gom-correlate.html). In the optical DIC analysis, the ε_{xx} engineering strain component (parallel to the loading axis) was utilized to represent the local strain through the gauge section of the tensile specimen. A virtual extensometer was adopted in the DIC analyses to measure the elongation for obtaining the engineering stress-strain curve. Static synchrotron X-ray diffraction experiment was carried out at beamline 11ID-C, Argonne National Laboratory, Chicago, USA (beam wavelength: 0.1173 Å). The acquired two-dimensional diffractogram was integrated at 5° azimuthal sectors respectively along the RD (87.5-92.5°) and the transverse direction (TD, -2.5-2.5°) using a GSAS-II open-access software (Toby and Von Dreele, 2013) to obtain one-dimensional diffraction patterns. Individual phase properties were investigated using a Hysitron Tribo nanoindentation with a Berkovich tip which was calibrated on a standardized fused-quartz specimen. A maximum 1000 μN load was applied in each indent with a load function consisting of a 10 s loading unit and a 5 s holding duration at the peak contact force. The load-displacement curves were analyzed by the Oliver-Pharr approach (Pharr and Bolshakov, 2002; W.C. Oliver; G.M. Pharr, 1992) to determine the nano hardness as well as

the elastic modulus values. A PI-88 Hysitron Picoindenter was also employed for quasi-in-situ investigation of nano hardness for the strain localization region. In the SEM-based nanoindentation experiment a conical tip was adopted and was also calibrated on a standardized fused-quartz before measurement. The maximum load was also kept at 1000 μN in the monolithic measurement.

2.2 In-situ microstructure-based strain mapping

An in-situ microstructure-based digital image correlation approach (Yan et al., 2015) was employed to quantitatively assess the heterogeneous strain accommodation and evolution during plastic deformation. Following our previous experimental recipes (Rui et al., 2019; Wei et al., 2021, 2020), speckle patterns were coated on mirror-finished tensile specimens (gauge dimension kept the same as ex-situ testing) by using ~40 nm diameter colloidal SiO_2. These coated specimens were then dried in flow air with sprayed ethanol to achieve desirably homogenous patterns (see Supplementary Fig. S1 as an example). During the in-situ tensile experiment, BSE, SE, in-beam BSE, and in-beam SE micrographs with 4096×4096 resolution (41.5×41.5 μm^2 field of view) were recorded every 1.0-1.5% engineering strain incrementation, and the in-beam SE micrographs were subjected to DIC calculation for strain determination in a commercial GOM software (https://www.gom.com/en/products/gom-correlate). The square facet size applied for DIC analysis was 60 pixel, giving rise to a spatial resolution of about 600 nm, which was approximately 30 % the average grain size of the β-phase. The inter-facet distance was set as ~200 nm, in equivalent to 20 pixel under the current imaging condition. Since the local strain value determined from DIC analysis may exhibit a dependency on the applied subset size, we have validated that the adopted 60 pixel (in equivalent, about 600 nm) subset size exhibits negligibly small influence in the strain calculation results. Detailed analyses can be found in Supplementary Note 1. Because of the quantitative analyses in the present work involve strain profile acquisition along certain directions as well as distribution assessments, and the physical conclusions drawn should be frame-indifferent (Gurtin et al., 2010), the von Mises equivalent strain is therefore adopted. Considering the thin-sheet geometry of the present tensile specimen (thickness ~1.0 mm), a plane stress approximation was applied, which states:

$$\boldsymbol{\varepsilon}_{\mathrm{p}} = \frac{1}{2}[\nabla \boldsymbol{u} + (\nabla \boldsymbol{u})^{\mathrm{T}}] \simeq \begin{bmatrix} \varepsilon_{xx} & \varepsilon_{xy} & 0 \\ \varepsilon_{xy} & \varepsilon_{yy} & 0 \\ 0 & 0 & -\varepsilon_{xx} - \varepsilon_{yy} \end{bmatrix} \quad (1)$$

In Eq. (1), $\boldsymbol{\varepsilon}_{\mathrm{p}}$ is the plastic strain tensor under the plane-stress presumption, $\boldsymbol{u}$ represents the displacement field which is measured by μ-DIC. The out-of-plane strain component ε_{zz}, was determined using the principle of volume constancy: $\mathrm{tr}(\boldsymbol{\varepsilon}_{\mathrm{p}}) = 0$. The von Mises equivalent strain, which is then an in-plane frame-indifferent scalar, is calculated by:

$$\varepsilon_{\mathrm{VM}} = \sqrt{\frac{2}{3}\boldsymbol{\varepsilon}_{\mathrm{p}} : \boldsymbol{\varepsilon}_{\mathrm{p}}} \quad (2)$$

Note that, since the present study primarily concerns about deformation at relatively high plastic strain levels, the elastic compressibility of the present alloy would then have negligible effect on most of the results. However, in the elastoplatic transition region, given the high yield strength (Fig. 2), $\varepsilon_{\mathrm{VM}}$ calculated at ~2.6 % total strain (the first data point of the in-situ results) may contain a relatively high portion of elastic strain.

The plastic strain distributions for α- and β-phases were obtained by segmenting the two-dimensional strain maps using the in-beam BSE contrast of the two phases, which presumably imposes the minimum amount of manipulation to the original dataset. The acquired BSE micrographs and EBSD measurement were utilized for slip trace analysis via a home-built STrCryst program (https://github.com/shaolouwei/STrCryst) in which the theoretical slip trace was calculated as (Wei et al., 2021):

$$\mathbf{t} = (\boldsymbol{G}^{-1} \cdot \mathbf{n}) \times \mathbf{N} \tag{3}$$

where $\mathbf{n}$ and $\mathbf{N} = [001]$ denote the unit slip/twin (crystal frame) and observant plane (specimen frame) normals, and $\boldsymbol{G}$ represents the coordinate transformation matrix (Bunge, 1982):

$$\boldsymbol{G} = \begin{bmatrix} \cos\varphi_1\cos\varphi_2 - \sin\varphi_1\sin\varphi_2\cos\phi & \sin\varphi_1\cos\varphi_2 + \cos\varphi_1\sin\varphi_2\cos\phi & \sin\varphi_2\sin\phi \\ -\cos\varphi_1\sin\varphi_2 - \sin\varphi_1\cos\varphi_2\cos\phi & -\sin\varphi_1\sin\varphi_2 + \cos\varphi_1\cos\varphi_2\cos\phi & \cos\varphi_2\sin\phi \\ \sin\varphi_1\sin\phi & -\cos\varphi_1\sin\phi & \cos\phi \end{bmatrix} \tag{4}$$

In Eq. (4), $(\varphi_1,\ \phi,\ \varphi_2)$ are Euler angles following the Bunge's convention (Bunge, 1982) that can be exported for certain α- and β- phases from the corresponding EBSD measurements. It should be noted that in these calculations, a coordinate transformation is necessary. Vector $[u\ v\ t\ w]$ on $(h\ k\ i\ l)$ plane expressed in hexagonal coordinate is transformed to Cartesian coordinate via (Bunge, 1982): $[u'\ v'\ w'] = [(2u+v)\sqrt{3}/2 \quad 3v/2 \quad wr_{c/a}]$ and $(h'\ k'\ l') = ((2h+k)\sqrt{3}/3 \quad k \quad l/r_{c/a})$. The c-to-a ratio ($r_{c/a}$) for the present alloy is determined using synchrotron X-ray diffractometry as described in Section 2.1. Owing to the fact that surface quality may potentially bring about artifacts (e.g. surface scratches from specimen preparation) to the slip trace analysis, the presence of slip trace was verified by step-wise titling the specimen for ±15°. It is also noted that a ±10° alignment deviation tolerance (Cepeda-Jiménez et al., 2016; Wei et al., 2021) was applied when comparing the actual and the theoretical slip traces.

3. Results

3.1 Microstructure and mechanical response under uniaxial tensile loading

The investigated Ti-Al-V-Fe alloy exhibits a two-phase microstructure with near-equiaxed HCP α-phase (grain size ~4 μm) and BCC β-phase (grain size ~2 μm). EBSD phase map (Fig. 1 (b)) reveals ~87.6% α-phase and ~12.4% β-phase, which is

also confirmed from the synchrotron X-ray measurements (Fig. 1 (e)). ESBD inverse pole figure acquired along the loading direction (IPF, Fig. 1 (a)) together with pole figures (PFs, Fig. 1 (c)) taken with respect to $\{0001\}$, $\{10\bar{1}0\}$, and $\{11\bar{2}0\}$ poles confirm that the present alloy shows a pronounced rolling texture (Bridier et al., 2008; Chan and Koss, 1983) where the c-axes of the HCP lattices are mostly aligning perpendicular to the RD (deviation within ±15°). EDS line profile acquired across anα/β interface demonstrates the enrichment of V and Fe and the depletion of Ti and Al in the β-phase (Fig. 1 (d)). As a result of the strong rolling texture, clear distinctions in the peak intensity of the α-phase can be observed from the one-dimensional synchrotron X-ray diffraction profiles for RD and TD. Lattice constants of α- and β- phases are determined as $a_\alpha = 2.9366$ Å, $c_\alpha = 4.6828$ Å; and $a_\beta = 3.2254$ Å through Rietveld refinement of the diffraction patterns (calculation error $R_{wp} < 5$ % was achieved (Young et al., 1982)). It is also recognized that the c-to-a ratio of the α-phase achieves $r_{c/a} = 1.5946$, appearing slightly larger than that of commercially pure Ti ($r_{c/a}$~1.58) (Nayak et al., 2018; Wood, 1962), which signifies the potential effect of Al, V, and Fe dissolution.

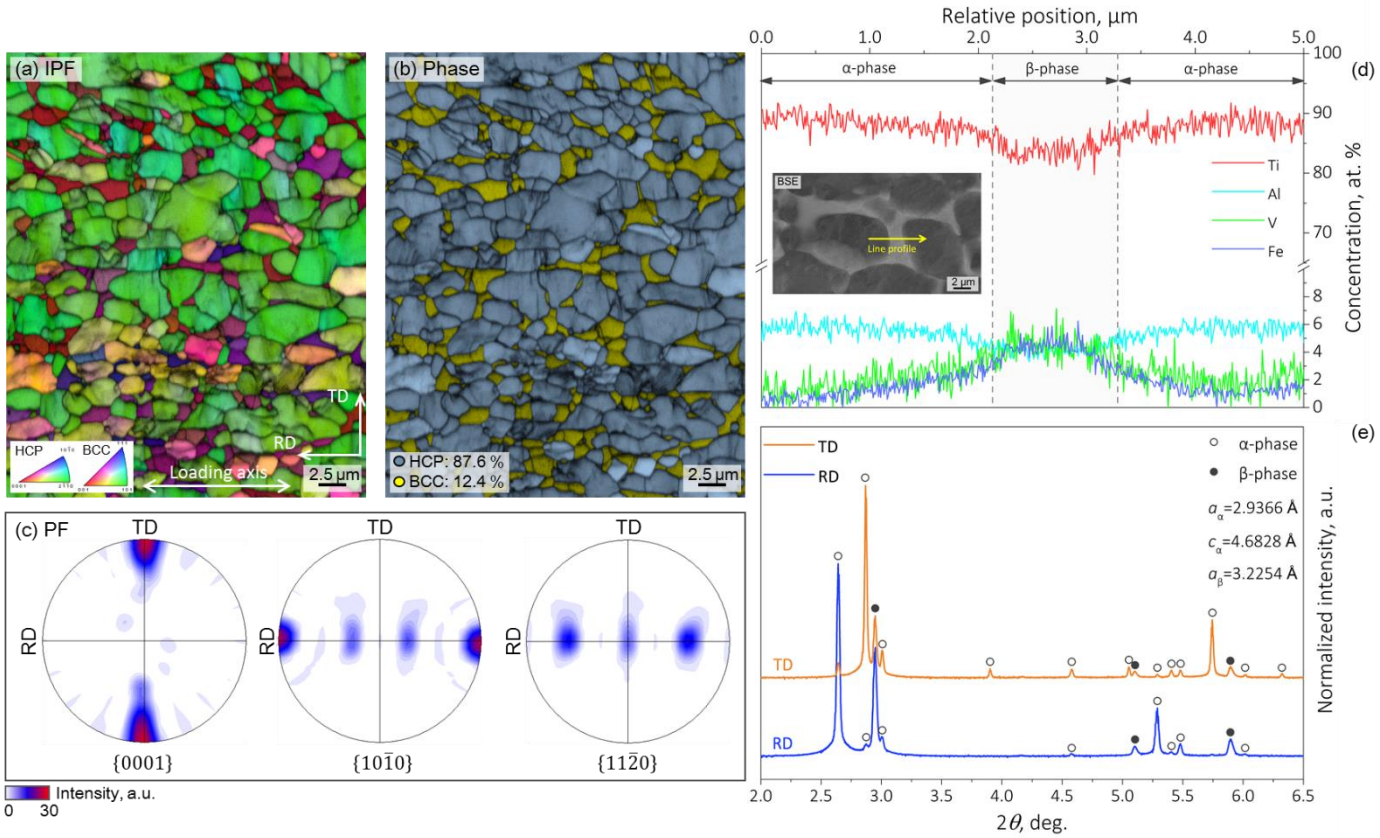

Fig. 1 | Microstructure of the Ti-Al-V-Fe alloy at the undeformed state: *(a) IPF acquired along the loading direction (parallel to RD); (b) EBSD phase map; (c) representative pole figures obtained from* $\{0001\}$, $\{10\bar{1}0\}$, *and* $\{11\bar{2}0\}$ *poles; (d) elemental distribution across α/β PB revealed by EDS line scan; (e) synchrotron X-ray diffraction patterns acquired at RD and TD for lattice constants determination. The full two-dimensional diffractogram is provided in Supplementary Fig. S2.*

Ex-situ uniaxial tensile testing performed along the RD shows that the present Ti-Al-V-Fe alloy yields at ~1034 MPa (Fig. 2 (a)) then strain-hardens (Fig. 2 (a)), achieving an ultimate tensile strength (UTS) of ~1150 MPa. The uniform elongation determined by the Considère criterion is ~6.9% (Fig. 2 (b)) while the eventual fracture elongation reaches ~15.9%. Inset in Fig. 2 (a) demonstrates the local strain ($\varepsilon_{loc.}$) profiles acquired along the middle section of the specimen at the necking point

and one frame before macroscopic fracture. The maximum local strain reaches ~45.4 % across the specimen gauge before final fracture. It should be noted that since the present tensile test was carried out on thin sheet specimen (actual thickness ~1.0 mm) there could be pronounced out-of-plane strain at high deformation level which cannot be resolved by the two-dimensional optical DIC technique. While the present tensile engineering strain is acquired utilizing the ε_{xx} engineering strain component (parallel to the loading axis), it is worthwhile highlighting that the application of three-dimensional optical DIC technique can enable a full-field strain measurement in future work.

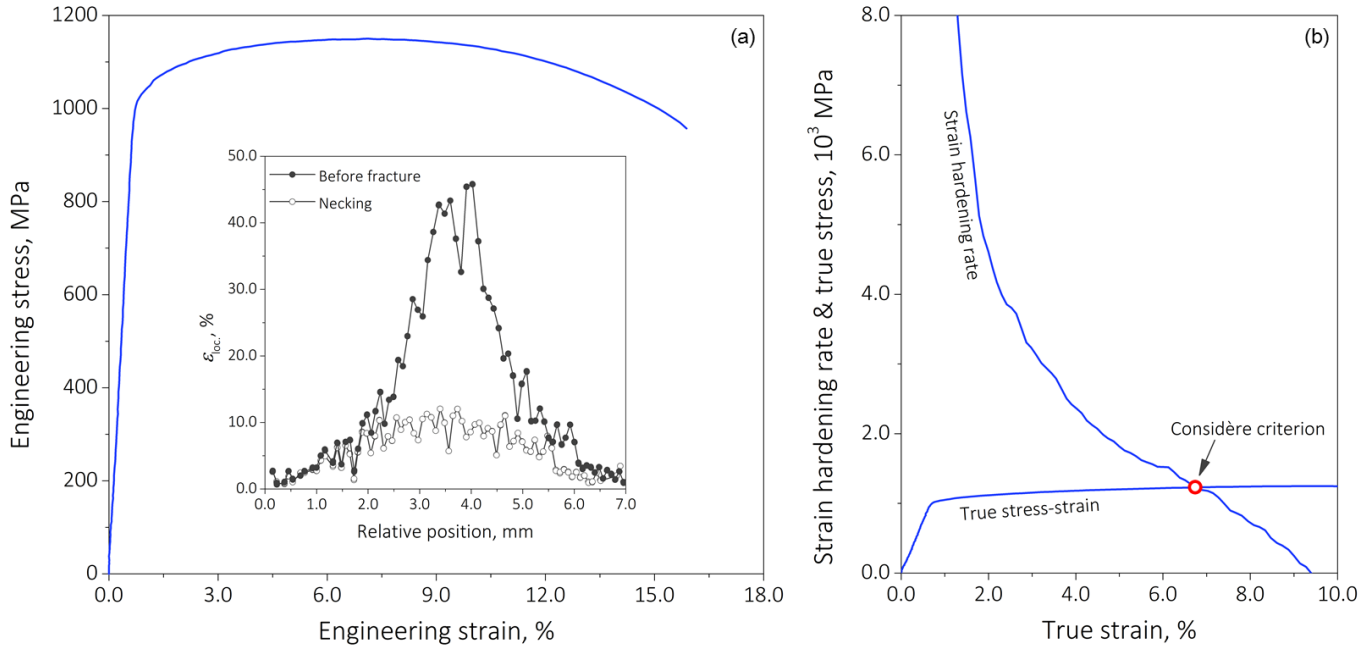

Fig. 2 | Mechanical response under uniaxial tensile loading: *(a) engineering stress-strain curve; (b) strain hardening rate. Inset of (a) presents the local strain profile at the necking point (determined by the Considère criterion) and one frame before macroscopic fracture. Here the ε_{xx} engineering strain component (parallel to the loading axis) is utilized to represent the local strain level across the gauge section of the specimen. The spatial resolution of the optical DIC utilized in these measurements is ~140 pixel/mm. Square facet size and inter-facet distance employed in the strain calculation are ~0.14 mm (20 pixel) and ~0.07 mm (10 pixel).*

3.2 In-situ microstructure-based strain mapping

To examine the heterogeneous plastic strain accommodation and thereby its evolution characteristics at the microstructural level, in-situ μ-DIC analyses were carried out in a selected area of interest with 41.5×41.5 μm^2 field of view. As shown in Fig. 3 (a), the α- and β-phases within this area are homogenously distributed without significant phase clustering. Fig. 3 (b)-(h) demonstrate the two-dimensional local strain ($\varepsilon_{loc.}$) distribution evolution with respect to increasing applied global plastic strain level ($\varepsilon_{app.}$). Here, the von Mises equivalent strain definition is employed to study the local strain evolution. At moderate deformation levels (Fig. 3 (b)-(d)), while the majority of the microstructural constitutes only accommodate mild plastic strain, conspicuous strain localization bands nucleate (see white arrows in Fig. 3 (b)). The DIC data suggests that the propagation of these band are not significantly influenced by the presence of α/β PBs (Fig. 3 (c) and (d)). A closer examination reveals the following two main features: (1) the peak strains within these bands appear significantly higher than the corresponding applied global strain levels and their microstructural adjacencies (for detailed quantifications see Fig. 4 (a)-(c)); and (2) the strain

localization bands developed within the field-of-view exhibit high inclination angles close to ~80° with respect to the horizontal loading axis (detailed statistical analyses are provided in Fig. 4 (d)). As plastic straining proceeds (Fig. 3 (e)-(h)), the strain localization persists and evidently intensifies in the same sites observed in Fig. 3 (b)-(d), emerging into prominent connected bands ($\varepsilon_{loc.} > 50.0$ %) that develop throughout the entire monitored region. In contrast to these pronounced strain localization features, the $\varepsilon_{loc.}$ accommodated by the rest of the microstructure (i.e. regions outside the bands) exhibits a relatively homogenous tendency. It is worthwhile noting that at the even higher deformation levels (Fig. 3 (g) and (h)) μ-DIC pixel loss starts to appear within the two most pronounced strain localization bands, signifying the potential onset of damage nucleation or surface cracking. Although this sort of phenomenon could also be induced by the surface relief during plastic deformation that abates the μ-DIC pattern quality (Maraghechi et al., 2019; Sutton and Hild, 2015), detailed damage investigation presented in Section 4.3 does validate the directional correlation between strain localization bands and governing micro-damage incidents. A more detailed exploration of the foregoing strain localization effect will be discussed next, starting with quantitative assessments of two representative bands (see the annotations in Fig. 3 (h)).

Studying Fig. 4, it is recognized from the local strain profile of strain localization band 1 that the $\varepsilon_{loc.}$ value demonstrates a drastic increase upon the macroscopic yielding of the alloy far exceeding the $\varepsilon_{loc.}$ of its vicinity in the 0.0-12.3 % applied global strain range. Two physical parameters, the peak strain and the width of the strain band are employed in the present study to better quantify the evolution features of strain localization. Note that the strain localization band width here is determined as the full width at half maximum (FWHM) of the Gaussian regression fitting of the corresponding strain profile. In these analyses, at least 10 strain points across the strain localization bands are subjected to the regression analysis, and the fitting errors in the adopted Levenberg-Marquardt algorithm were presented as error bars in Fig. 4 (c). More details of the calculation and verification of the subset size selection are provided in Supplementary Fig. S4 and Supplementary Note 1. During acquisition of these two line profiles and the proceeding calculation of the two parameters, it has been confirmed that the horizontal profiles do not intersect with additional α/β phase boundary outside the strain localization bands. As seen in Fig. 4 (c), the peak $\varepsilon_{loc.}$ undergoes a power function-like increase with respect to the increasing applied global strain level, reaching up to ~81.6% at only ~12.2% global strain in Band 1. The resultant band width, however, almost persists at ~0.94 μm upon its formation, regardless of the macroscopic deformation level, despite a subtle increase occurs at ~6.0 % global strain and onwards. Similar trends are also present in Band 2 subjected to the analysis (Fig. 4 (b)): its peak local strain achieves ~99.1 % at ~12.2% global strain while maintaining a confined width that varies between 1.1-1.4 μm (Fig. 4 (c)).

The second conspicuous feature of the observed strain localization bands lies in the fact that they seemingly develop high inclination angle close to ~80° with respect to the horizontal loading axis (Fig. 3 (d)-(h)). To provide a statistically reliable quantification of this geometric characteristic, the fractured in-situ testing specimen was subjected to post-mortem SE-imaging. Four 100×100 μm^2 areas with increasing distance from 1.50 mm to 2.25 mm to fracture end were analyzed. Within each

100×100 μm^2 area, the inclination angles of at least 20 strain localization bands were measured (the raw dataset is summarized in Supplementary Table S1). Fig. 4 (d) comparatively demonstrates the cumulative frequency distribution for the strain localization band inclination angles obtained in four regions. It is evident that regardless of the distance from the fracture end, almost all data points accumulate in the inclination angle range of 80-90^o, which is compatible with the in-situ results shown in Fig. 3. This sort of characteristic is also clearly seen in the inset of Fig. 4 (d), in which the arithmetical average of inclination angle calculated in each 100×100 μm^2 region almost maintain the same value given their different distances from the fracture end. Compared with the well-known mechanisms for strain localization that highlight the importance of maximum shear stress at a 45^o inclination angle during a uniaxial tensile test (Barbe et al., 2009), these analyses indicate that the present strain localization features exhibit a strong correlation with preferential slip system activation spanning over the entire microstructure.

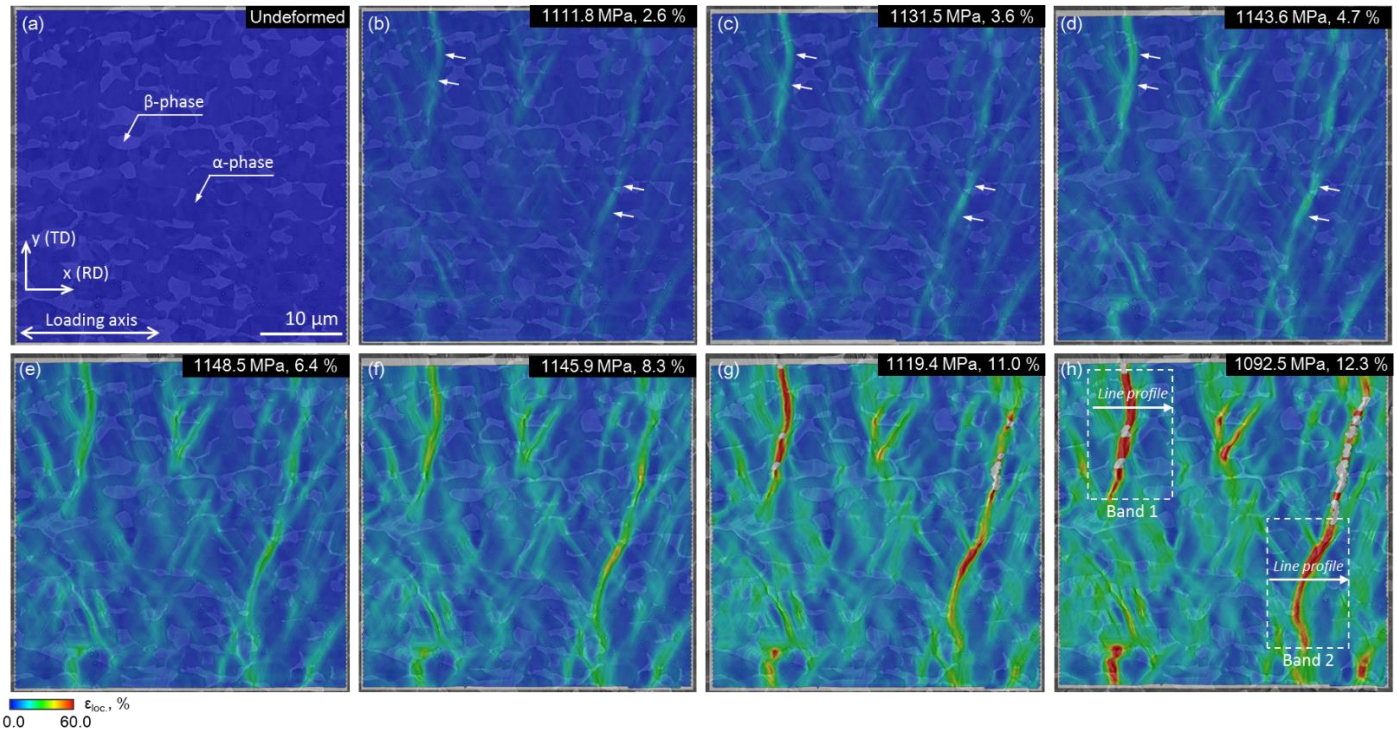

Fig. 3 | Microstructure-based strain mapping results: *(a) selected area of interest at the undeformed state; (b)-(h) local strain (von Mises equivalence) evolution with respect to increasing plastic straining level. The corresponding engineering stress and strain values are denoted at the top right corner in each micrograph. Two representative long-range strain localization bands are subjected to further quantitative assessment. Complementary strain maps for* ε_{yy} *are provided in Supplementary Fig. S3. Facet size in (a)-(h) is 60 pixel, which corresponds to a spatial resolution of about 600 nm. The inter-facet distance was chosen as ~200 nm (20 pixel under the current imaging condition).*

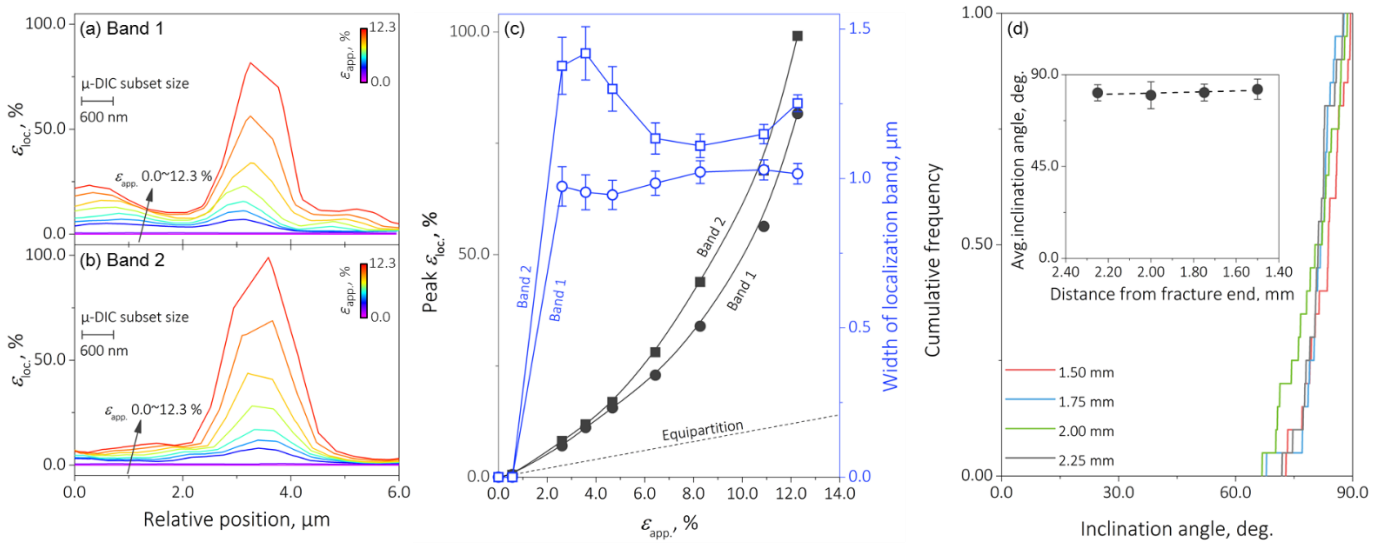

Fig. 4 | Formation and maturation of the two representative strain localization bands highlighted in Fig. 3: *(a) and (b) line profiles for local strain evolution across the bands with respect to increasing deformation level; (c) evolution of peak strain within the bands as well as the band widths; (d) statistical analysis of the inclination angle of strain localization band with respect to the horizontal loading axis. Inset of (d) shows the arithmetical average inclination angle in each 100×100 μm² region. Error bars in (c) represent the fitting error in the Levenberg-Marquardt algorithm applied for regression analyses. Error bars in the inset of (d) are the standard deviations.*

In the following discussion section, we will firstly explore the crystallographic characteristics for the operative deformation mechanisms observed within the strain localization region. Next, plastic strain accommodation between α- and β-phases and the corresponding evolution characteristics will be discussed based on statistical analysis of the μ-DIC maps and nano-mechanical testing results. Finally, we will identify the governing damage mechanism and elucidate its relevance to the various deformation micro-mechanisms.

4. Discussion

4.1 Slip inception, transfer, and its relation with strain localization

Typical strain localization origin in multi-phase alloys is ascribed to GBs or PBs (Bieler et al., 2014; Hoefnagels et al., 2015; Rui et al., 2019; Tasan et al., 2014b) because of plastic strain incompatibility intensification at these locations either due to crystallographic orientation (Bieler et al., 2019) or intrinsic phase properties (Dutta et al., 2019; Wei et al., 2021). However, the μ-DIC results in Fig. 3 clearly confirm that the strain localization bands neither follow the geometric alignment of α/β PBs nor do they terminate at GBs or PBs. Instead, these strain localization bands tend to propagate through α/β PBs (Fig. 3 (h)), leading to the maturation of long-range localization bands with tens of micrometer length (also see Fig. 7 (b2)).We suggest from a "*necessity*" point of view, the operative deformation micro-mechanisms within the strain localization regions are characterized by two important crystallographic features: first, extensive prismatic ⟨**a**⟩ slip activation owing to the texture; and second, smooth slip transfer between α- and β-phases.

Fig. 5 (a1)-(a3) demonstrates the slip trace analysis for strain localization band 1 in Fig. 3 at its pre-mature state, i.e. at a

comparatively moderate global strain level of ~2.6% (see Fig. 3 (b) as a guide). Here, the Schmid factor (SF) is exploited as a first-order indicator to assess the activation propensity for various dislocation gliding modes in the α-phase:

$$SF = [(\boldsymbol{G} \cdot \mathbf{f}) \cdot \mathbf{n}] \cdot [(\boldsymbol{G} \cdot \mathbf{f}) \cdot \mathbf{s}] \tag{5}$$

where $\boldsymbol{G}$, $\mathbf{f} = [010]^{\mathrm{T}}$, $\mathbf{n}$, and $\mathbf{s}$ are the coordinate transformation matrix (based on Eq. (4)), the far-field stress state (uniaxial tensile in the specimen frame), the unit vectors of slip plane normal and slip direction. Comparison between the typical slip traces developed within the microstructure (Fig. 5 (a1)) and the theoretically predicted ones clearly confirms the onset of evident prismatic $\langle\mathbf{a}\rangle$ slip in the α-phase. The corresponding SF values calculated based on Eq. (5) achieve 0.4285, 0.4387, and 0.4947 for these three slip traces respectively belong to $[10\bar{1}0](\bar{1}2\bar{1}0)$, $[01\bar{1}0](2\bar{1}\bar{1}0)$, and $[01\bar{1}0](2\bar{1}\bar{1}0)$ prismatic $\langle\mathbf{a}\rangle$ slip systems. In contrast to the initiation of slip delocalization events (such as multi-slip), the elevation of global applied strain, in fact, intensifies the onset of prismatic $\langle\mathbf{a}\rangle$ slip within these local sites, leading to the development of the eminent strain localization bands observed at the higher deformation levels (Fig. 3 (c)-(h)). It is also noteworthy that the consistent geometric agreement between the strain localization bands and the predicted prismatic $\langle\mathbf{a}\rangle$ slip traces throughout the investigated deformation levels also consolidates the mechanistic linkage between these two activities.

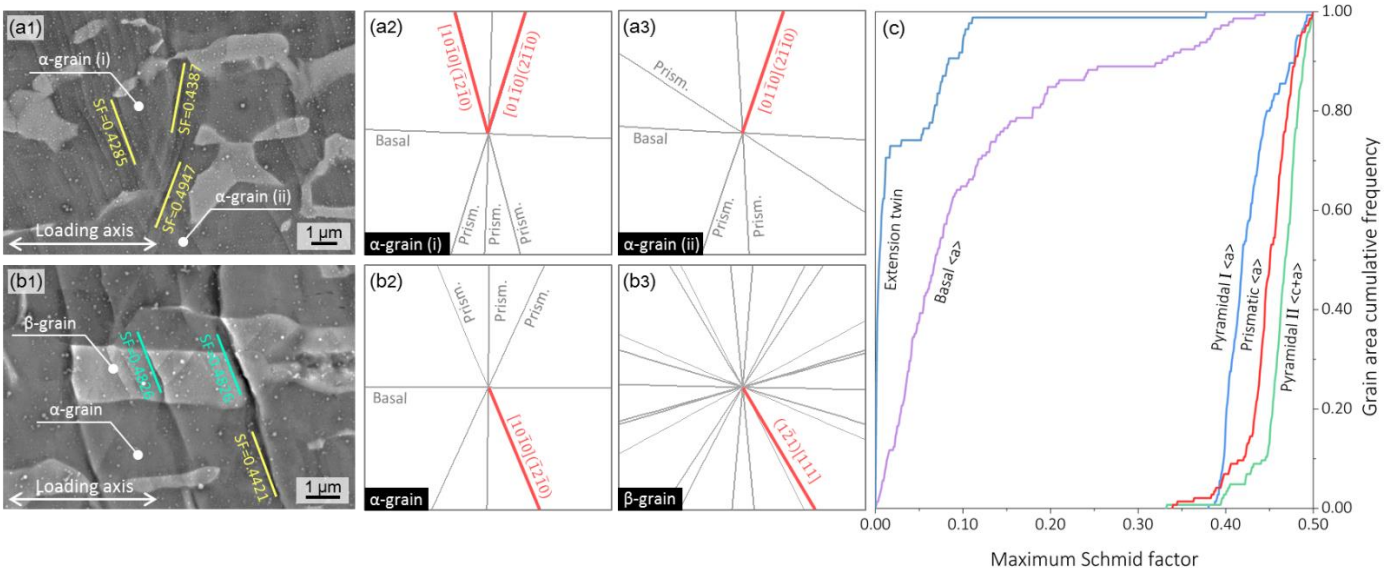

Fig. 5 | Slip trace analysis for understanding the inception of the strain localization bands: *(a1)-(a3) experimental results and theoretical prediction of slip trace in the α-phase; (b1)-(b3) presence of slip transfer across one typical α/β PB and the identification of the activated slip modes; (c) maximum Schmid factor distribution chart considering grain area fraction cumulative frequency. Abbreviation adopted: prismatic (prism.).*

The second conspicuous feature of these strain localization bands lies in their length-scales, which increase up to tens of micro-meter at a global strain level of ~12.3%, appearing evidently larger than the node-like strain localization features commonly present in dual-phase steels (Matsuno et al., 2015; Tasan et al., 2014b) or titanium alloys (Chong et al., 2020, 2019; Zheng et al., 2017b). Based on the texture characteristics revealed by the PFs (Fig. 1 (c)), we next perform a nonparametric SF values

assessment amongst basal $\langle \mathbf{a} \rangle$, prismatic $\langle \mathbf{a} \rangle$, pyramidal I-$\langle \mathbf{a} \rangle$, pyramidal II-$\langle \mathbf{c}+\mathbf{a} \rangle$ slip modes together with the $\{10\bar{1}2\}\langle 10\bar{1}\bar{1} \rangle$ extension twinning event across the microstructure. For better quantification of the texture effect, the raw cumulative distribution for the SF values has been modulated by the corresponding α-grain area (Fig. 5(c)). The calculation results indicate that the present texture tends to strongly suppress the onset of both basal $\langle \mathbf{a} \rangle$ slip and extension twin nucleation, whose grain area cumulative frequencies respectively reach ~0.92 and ~0.98 for $SF < 0.35$. In case of prismatic $\langle \mathbf{a} \rangle$, pyramidal I-$\langle \mathbf{a} \rangle$, and pyramidal II-$\langle \mathbf{c}+\mathbf{a} \rangle$ slip, on the other hand, all develop no more than ~0.20 cumulative grain area frequencies for $SF < 0.40$, signifying the geometrically-favored activation propensity. Interestingly, slip trace analyses carried out in more than 20 α-grains (see Table 1) demonstrate no trait of pyramidal I-$\langle \mathbf{a} \rangle$ or pyramidal II-$\langle \mathbf{c}+\mathbf{a} \rangle$ slip activation, while prismatic slip is much more predominant. This sort of activation behavior can be rationally understood from the perspective of the distinctive CRSS magnitude of the corresponding slip mode. Appreciable simulation and experimental effort carried out in α-Ti systems have confirmed that the CRSS for prismatic $\langle \mathbf{a} \rangle$ slip exhibits the lowest magnitude amongst all possible plastic deformation modes (Baudoin et al., 2019; Hémery et al., 2020; Ma et al., 2019; Warwick et al., 2012b), while CRSS magnitudes for basal $\langle \mathbf{a} \rangle$, pyramidal I-$\langle \mathbf{a} \rangle$, pyramidal II-$\langle \mathbf{c}+\mathbf{a} \rangle$ slip and extension twinning are all 1-2 times higher. It is therefore informative that provided the similar geometric favorability amongst prismatic $\langle \mathbf{a} \rangle$, pyramidal I-$\langle \mathbf{a} \rangle$, and pyramidal II-$\langle \mathbf{c}+\mathbf{a} \rangle$ slip due to texture, the intrinsically inferior resistance to plastic incipience of the prismatic $\langle \mathbf{a} \rangle$ slip system is account for its pronounced activation in the present alloy. Given the foregoing crystallographic analysis, it should be pointed out that the variation of texture can effectively alter the dominant slip mechanism that results in the long-range strain localization event. An exemplary investigation of a textured Ti64 alloy revealed the governing role of pyramidal $\langle \mathbf{c}+\mathbf{a} \rangle$ slip in strain localization inception, provided the lowest CRSS magnitude of prismatic $\langle \mathbf{a} \rangle$ slip (Echlin et al., 2016). However, more systematic future work deems necessary to bridge the different strain localization inception modes with the corresponding macroscopic load-bearing capacity.

We next focus on the propagation of these strain localization bands. In-situ μ-DIC results and BSE micrographs reveal that these bands are barely impeded by the presence of α/β PBs (Fig. 3 (e)-(h)), instead the elevating global strain level brings about long-range rectilinear strain localization bands that propagate throughout the entire monitored region. One such feature representatively demonstrated in Fig. 5 (b1)-(b3) shows that the slip traces in α- its adjacent β-phases exhibit nearly co-linear alignment, and trace calculation proves the onset of $[10\bar{1}0](\bar{1}2\bar{1}0)$ prismatic $\langle \mathbf{a} \rangle$ slip ($SF = 0.4421$) and $(1\bar{2}1)[111]$ slip ($SF = 0.4826$) in these two phases. The comparatively high SF values together with the compatible geometric alignment rationally signify a smooth deformation transfer procedure has taken place across the α/β PBs. Here, the Luster-Morris geometric compatibility parameter (m') is employed for further quantification of such a deformation transfer micro-event (Luster and Morris, 1995):

$$m' = \left[\left(\boldsymbol{G}_{\beta}^{-1} \cdot \mathbf{s}_{\beta}\right) \cdot \left(\boldsymbol{G}_{\alpha}^{-1} \cdot \mathbf{s}_{\alpha}\right)\right] \cdot \left[\left(\boldsymbol{G}_{\beta}^{-1} \cdot \mathbf{n}_{\beta}\right) \cdot \left(\boldsymbol{G}_{\alpha}^{-1} \cdot \mathbf{n}_{\alpha}\right)\right] \tag{6}$$

This parameter concerns about the alignment between the slip directions in α and β phases ($\mathbf{s}_\alpha$ and $\mathbf{s}_\beta$) as well as the alignment between the corresponding slip plane normals ($\mathbf{n}_\alpha$ and $\mathbf{n}_\alpha$). Following Eq. (6), the corresponding angles between $\mathbf{s}_\alpha$ and $\mathbf{s}_\beta$ as well as between $\mathbf{n}_\alpha$ and $\mathbf{n}_\alpha$ are also considered in the present calculation:

$$\kappa = \arccos\left[(\boldsymbol{G}_\beta^{-1}\cdot\mathbf{s}_\beta)\cdot(\boldsymbol{G}_\alpha^{-1}\cdot\mathbf{s}_\alpha)\right] \tag{7}$$

$$\psi = \arccos\left[(\boldsymbol{G}_\beta^{-1}\cdot\mathbf{n}_\beta)\cdot(\boldsymbol{G}_\alpha^{-1}\cdot\mathbf{n}_\alpha)\right] \tag{8}$$

In order to ensure statistical reliability, 25 such slip transfer events were subjected to the analyses and their crystallographic details are summarized in Table 1. In accord with the analysis discussed in Fig. 5 (b1)-(b3), all the sampled incidents fall into the regions with $SF > 0.40$, indicating the preferable geometric characteristic for their activation propensity (Fig. 6 (a)). The corresponding cumulative frequency curve (inset of Fig. 6 (a)) shows that slip activation in the β-phase exhibits a comparatively more disperse distribution especially in the $SF > 0.45$ regime, which is possibly due to the diverse slip systems (i.e. $\{110\}\langle 1\bar{1}1\rangle$, $\{112\}\langle 11\bar{1}\rangle$, and $\{123\}\langle 11\bar{1}\rangle$ slip systems, also see Fig. 6 (c)). The SF versus m' chart in Fig. 6 (b) reveals that all the surveyed slip transfer events populate in the region with $m' > 0.82$ and nearly 0.75 of the data points accumulate in the $m' > 0.90$ region, proving the geometrically-favored alignment between prismatic $\langle\mathbf{a}\rangle$ and β-phase slip systems. The relatively high SF and m' values, therefore, suggest that once prismatic $\langle\mathbf{a}\rangle$ slip manages to incept due to external plastic loading, its transfer into adjacent β-phase will scarcely experience any pronounced retardation. These kinds of geometric characteristics consequently intensify the strain localization effect brought about by the extensive prismatic $\langle\mathbf{a}\rangle$ slip activation discussed above, which in turn accounts for the propagation of strain localization bands at a larger length scale (Fig. 3 (g) and (h)). From a crystallographic perspective, on the other hand, this sort of smooth slip transfer across the α/β boundaries can effectively mitigate stress concentration because of the lacking in interfacial residual dislocation nucleation (Bieler et al., 2009; Eshelby et al., 1951; McMurtrey et al., 2014; Scholz, 1997), alleviating interfacial damage or cracking incipience especially in HCP-structured metals (Arul Kumar et al., 2016; Sun et al., 2019; Wei et al., 2019b; Yoo, 1981). In fact, our quantitative damage assessments confirm the minor role of interfacial damage events in the macroscopic failure process. More detailed discussion is included in Section 4.3.

Table1 | Crystallographic details for the survey slip transfer incidents across α/β PBs

No.	Dislocation slip in α-phase			Dislocation slip in β-phase			m'
	Orientation	Slip system	SF	Orientation	Slip system	SF	
1	(93.0°, 57.9°, 91.9°)	$(01\bar{1}0)[2\bar{1}\bar{1}0]$	0.4593	(197.5°, 114.4°, 51.3°)	$(10\bar{1})[111]$	0.4492	0.9761
2	(278.3°, 124.8°, 102.3°)	$(01\bar{1}0)[2\bar{1}\bar{1}0]$	0.4764	(127.2°, 78.3°, 169.1°)	$(110)[1\bar{1}\bar{1}]$	0.4664	0.9952
3	(265.5°, 89.8°, 96.5°)	$(01\bar{1}0)[2\bar{1}\bar{1}0]$	0.4751	(219.4°, 83.3°, 16.9°)	$(\bar{1}21)[11\bar{1}]$	0.4905	0.9491
4	(269.7°, 77.9°, 97.2°)	$(01\bar{1}0)[2\bar{1}\bar{1}0]$	0.4813	(219.4°, 83.3°, 16.9°)	$(\bar{1}21)[11\bar{1}]$	0.4905	0.9878
5	(93.1°, 68.0°, 270.0°)	$(01\bar{1}0)[2\bar{1}\bar{1}0]$	0.4417	(139.6°, 75.9°, 168.0°)	$(011)[11\bar{1}]$	0.4374	0.8778

6	(90.0°, 88.5°, 270.6°)	$(10\bar{1}0)[\bar{1}2\bar{1}0]$	0.4277	(142.0°, 59.4°, 178.1°)	$(12\bar{1})[\bar{1}11]$	0.4683	0.9795
7	(89.7°, 75.6°, 269.0°)	$(10\bar{1}0)[\bar{1}2\bar{1}0]$	0.4421	(318.7°, 106.4°, 21.0°)	$(1\bar{2}1)[111]$	0.4826	0.9658
8	(271.3°, 111.1°, 93.0°)	$(10\bar{1}0)[\bar{1}2\bar{1}0]$	0.4091	(226.0°, 103.7°, 346.7°)	$(110)[1\bar{1}\bar{1}]$	0.4271	0.8691
9	(271.5°, 107.6°, 91.6°)	$(01\bar{1}0)[2\bar{1}\bar{1}0]$	0.4424	(282.9°, 19.9°, 123.6°)	$(213)[11\bar{1}]$	0.4348	0.9855
10	(271.8°, 110.6°, 91.5°)	$(01\bar{1}0)[2\bar{1}\bar{1}0]$	0.4400	(282.9°, 19.9°, 123.6°)	$(213)[11\bar{1}]$	0.4348	0.9769
11	(268.8°, 111.5°, 86.8°)	$(10\bar{1}0)[\bar{1}2\bar{1}0]$	0.4549	(320.5°, 114.3°, 293.6°)	$(1\bar{1}0)[\bar{1}11]$	0.4195	0.9231
12	(269.6°, 125.7°, 88.4°)	$(10\bar{1}0)[\bar{1}2\bar{1}0]$	0.4444	(320.5°, 114.3°, 293.6°)	$(1\bar{1}0)[\bar{1}11]$	0.4195	0.8379
13	(273.7°, 105.4°, 88.2°)	$(10\bar{1}0)[\bar{1}2\bar{1}0]$	0.4535	(145.2°, 72.7°, 165.7°)	$(\bar{1}21)[11\bar{1}]$	0.4874	0.9748
14	(93.2°, 81.7°, 271.5°)	$(01\bar{1}0)[2\bar{1}\bar{1}0]$	0.4477	(229.9°, 98.7°, 347.4°)	$(12\bar{1})[\bar{1}11]$	0.4863	0.9779
15	(274.4°, 93.9°, 87.4°)	$(10\bar{1}0)[\bar{1}2\bar{1}0]$	0.4534	(229.9°, 98.7°, 347.4°)	$(12\bar{1})[\bar{1}11]$	0.4863	0.9719
16	(274.3°, 84.5°, 88.0°)	$(01\bar{1}0)[2\bar{1}\bar{1}0]$	0.4162	(141.8°, 83.1°, 172.4°)	$(13\bar{2})[\bar{1}11]$	0.4703	0.9757
17	(94.1°, 86.6°, 271.7°)	$(10\bar{1}0)[\bar{1}2\bar{1}0]$	0.4130	(141.8°, 83.1°, 172.4°)	$(13\bar{2})[\bar{1}11]$	0.4703	0.9823
18	(89.2°, 80.0°, 276.0°)	$(01\bar{1}0)[2\bar{1}\bar{1}0]$	0.4747	(137.2°, 84.2°, 173.5°)	$(\bar{1}21)[11\bar{1}]$	0.4698	0.9985
19	(270.4°, 109.4°, 89.4°)	$(10\bar{1}0)[\bar{1}2\bar{1}0]$	0.4392	(225.8°, 101.7°, 348.0°)	$(110)[1\bar{1}\bar{1}]$	0.4245	0.8847
20	(270.7°, 107.3°, 89.5°)	$(10\bar{1}0)[\bar{1}2\bar{1}0]$	0.4390	(225.8°, 101.7°, 348.0°)	$(110)[1\bar{1}\bar{1}]$	0.4245	0.8688
21	(270.8°, 114.1°, 89.5°)	$(10\bar{1}0)[\bar{1}2\bar{1}0]$	0.4391	(225.2°, 104.1°, 345.3°)	$(12\bar{1})[\bar{1}11]$	0.4660	0.9866
22	(274.1°, 108.3°, 92.3°)	$(10\bar{1}0)[\bar{1}2\bar{1}0]$	0.4220	(86.5°, 162.8°, 308.1°)	$(112)[11\bar{1}]$	0.4633	0.9912
23	(266.0°, 104.5°, 271.4°)	$(01\bar{1}0)[2\bar{1}\bar{1}0]$	0.4504	(178.3°, 67.8°, 301.9°)	$(\bar{1}12)[1\bar{1}1]$	0.4537	0.9976
24	(266.6°, 107.7°, 270.2°)	$(01\bar{1}0)[2\bar{1}\bar{1}0]$	0.4420	(178.3°, 67.8°, 301.9°)	$(\bar{1}12)[1\bar{1}1]$	0.4537	0.9915
25	(90.7°, 74.0°, 272.6°)	$(01\bar{1}0)[2\bar{1}\bar{1}0]$	0.4552	(225.3°, 96.1°, 350.7°)	$(12\bar{1})[\bar{1}11]$	0.4835	0.9888

As the last point to finalize the geometric compatibility discussion for slip transfer between α- and β- phases, the ψ versus κ diagram (Fig. 6 (c)) is also calculated for all the sampled incidents. It is recognized that a systematically greater tolerance exists in the alignment between slip planes: a more disperse distribution presents in the $0^o < \psi < 35^o$ range, while the corresponding slip directions alignment is more stringently confined in the $0^o < \kappa < 12^o$ range. This sort of correlation was also reported in slip-twinning transfer (Bieler et al., 2014; Wang et al., 2010) as well as twinning-twinning transfer (Arul Kumar et al., 2016) analyses in HCP-structured metals. A rational mechanism could be that upon the intersection between the incident slip activity and α/β PBs, the receiving grain would be able to adjust its spatial geometry (for example, via in-plane lattice rotation (Rui et al., 2019)) in a way such that the imposed trace can be more compatibly accommodated. While more dedicated crystal plasticity simulation efforts are necessary to consolidate this phenomenological postulation, recent three-dimension stereological characterizations (Fernández et al., 2013; Nervo et al., 2016) do imply its crystallographic validity. Amongst the surveyed slip incidents in the β-phase, the $\{112\}\langle 11\bar{1}\rangle$ slip system shows the relatively higher activity (13 incidents) compared with either the $\{110\}\langle 1\bar{1}1\rangle$ (8 incidents) or the $\{123\}\langle 11\bar{1}\rangle$ slip system. This, however, is in contrast with the α/β slip transfer study reported in a Ti-5Al-2.5Sn wt.% alloy (Seal et al., 2012) in which the $\{110\}\langle 1\bar{1}1\rangle$ and the $\{112\}\langle 11\bar{1}\rangle$ slip systems were equally activated. Although the experimental CRSS magnitudes for the β-phase appear rather lacking in the literature (Hémery et al., 2020), present data based on self-consistent crystal plasticity simulation (Deka et al., 2006; Venkatramani et al., 2007; Warwick et al., 2012a; Zhang et al., 2016) tend to systematically suggest only around tens of MPa higher CRSS for the $\{112\}\langle 11\bar{1}\rangle$ slip system compared with the $\{110\}\langle 1\bar{1}1\rangle$ slip system. As a result of this, it can be deduced that potential deviation of the local stress state from the far-field uniaxial tensile condition (mostly due to prismatic $\langle \mathbf{a} \rangle$ slip inception in the α-phase) may plausibly increase the resolved shear stress on the $\{112\}\langle 11\bar{1}\rangle$ slip system, facilitating

its activity. Finally, it is also worthwhile noting that some slip traces observed in the β-phase reveal wavy morphologies, which could be resulting from the well-documented pencil glide nature (Gilormini et al., 1988) of the screw dislocations in BCC-structured phase that leads to cross-slip. Under this kind of scenario, further TEM observation is deemed valuable in future investigations to quantitatively identify the actual property of the dislocations in the β-phase.

In light of the previous analyses that evidence the favorable slip transferability between α- and β-phases, further quantifications were performed to reveal the correlation between this kind of crystallographic property and the development of the long-range strain localization band. A representative BSE micrograph (acquired at ~1.50 mm from the fracture end) shown in Fig. 7 (a) cross-confirms the penetrative characteristics of the strain localization band as detailed in Figs. 3 and 5. Specifically, within this band which is about 19.57 μm in length, three β-grains are segmented (see the yellow boxes). The change in the band's alignment through its entire length is moderate, being compatible with the smooth slip transfer mechanisms discussed in Fig. 6. In order to better quantify such a correlation and considering the geometric property, two microstructural parameters are introduced in the assessments demonstrated below. First, $\overline{L_D}$, which is the arithmetical average length of all the surveyed strain localization bands at a distance D with respect to the fracture end (Fig. 7 (b2)). A larger $\overline{L_D}$ indicates that the strain localization band tends to cover a longer range in the microstructure. Second, $\overline{F_D}$, which is the arithmetical average line segmental fraction of the β-grain in the strain localization bands at a distance D with respect to the fracture end. As sketched in Fig. 7 (c1), $\overline{F_D}$ is obtained by measuring the cumulative portion of the β-grain segment f_i in the stain localization band. Thus, a larger $\overline{F_D}$ implies the higher fraction of β-grain involved in the strain localization band. To ensure statistical reliability, similar to the approach in Fig. 4 (c), a total of sixteen 100×100 μm^2 regions with increasing distance to the fracture end in the fractured in-situ specimen were subjected to electron microscopy study. Each $\overline{L_D}$ and $\overline{F_D}$ value is obtained from analyzing at least 20 strain localization bands ($N = 20$ for the equations in Fig. 7 (b1) and (c1)), and their evolutionary characteristics are respectively shown in Fig. 7 (b2) and (c2).

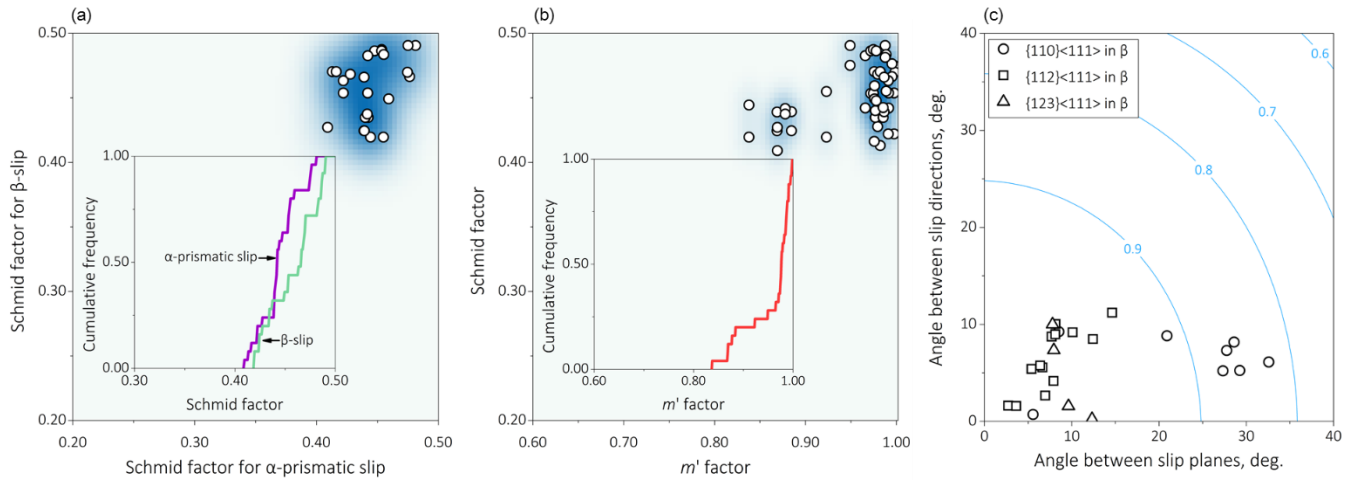

Fig. 6 | Non-parametric assessment of slip transferability between α- and β- phases: *(a) Schmid factor distribution chart for α-prismatic slip versus β-slip; (b) the Luster-Morris m' factor versus Schmid factor for all surveyed incidents; (c) geometric correlation chart concerning the angle between slip planes and slip directions. Insets in (a) and (b) exhibit the cumulative*

distribution frequency for the corresponding data points.

In line with the in-situ observations in Fig. 3, $\overline{L_D}$ exhibits a monotonic increasing trend from ~9.00 μm to 21.80 μm as the analyzed region approaches the fracture end (Fig. 7 (b2)). Such magnitudes of $\overline{L_D}$, if compared with the average grain sizes of α- and β-phases, which respectively achieves ~4 μm and ~2 μm (Fig. 1), are persuasive in confirming the long-range propagation feature of the strain localization bands. The statistical results in $\overline{F_D}$ show that the segmental fraction of the β-grain initially achieves ~0.15, then gradually increases up to ~0.23 when approaching the fracture end (Fig. 7 (c2)). That stated, the strain localization bands have indeed propagated through a discernible amount of β-grains, again suggesting the presence of smooth slip transfer between α- and β-phases. From a microstructural viewpoint, a reasonable comparison could be between $\overline{F_D}$ and the average β-phase line segmental content, $\overline{C_\beta} = 0.24 \pm 0.03$, measured from the undeformed microstructure (50 μm sampling lines were utilized). It is seen from Fig. 7 (c2) that a greater difference between $\overline{F_D}$ and $\overline{C_\beta}$ tends to occur in regions that are farther away from the fracture end, where the local plastic deformation level is presumably low. This sort of characteristic is indicative that the elevation of plastic deformation tends to enable strain localization bands to propagate in a more non-selective manner, which could be because the resolved shear stress is sufficiently high to active both the prismatic ⟨**a**⟩ slip in the α-phase and the accommodating slip systems in the β-phase. Although the results displayed in Fig. 7 (c2) primarily focus on the strain localization bands segmenting as least one β-grain, strain localization bands also develop in regions where β-phase is absent or the local content is lean. The presence of the latter phenomenon, although less evident than the α-β slip transfer mechanism explored before, is more frequently observed when the deformation level is moderate. From a crystallographic standpoint, it is rational to deduce that the incipience of long-range strain localization phenomenon with less (or no) β-grain involvement could be ascribed to two plausible mechanisms: first, easier slip transfer between prismatic ⟨**a**⟩-to prismatic ⟨**a**⟩ slip transfer between adjacent α-grains than α-β slip transfer; and second, the moderate deformation level does not surpass the CRSS of the corresponding slip systems in the β-phase, but is already sufficient to active eminent prismatic ⟨**a**⟩ slip in the α-phase (Hémery et al., 2020). To more accurately compare the dominance of these two possibilities, quantitative determination of the exact CRSS magnitudes for all slip systems is deemed necessary for future work. A final remark for the analyses in Fig. 7 lies in the potential limitations of the two-dimensional electron microscopy method exploited. Especially, the parameter $\overline{F_D}$, which resembles the grain size determination based on linear intersection (ASTM, 2013), is largely deficient in resolving the three-dimensional periodicity characteristic of the strain localization bands, as predicted by CPFEM simulation (Barbe et al., 2009; Flipon et al., 2020). A full-field characterization and quantification of the spatial features of the strain localization bands could be feasible via combined three-dimensional DIC and high-energy X-ray microscopy approaches (Abdolvand et al., 2018; Cherukara et al., 2018; Yu et al., 2021).

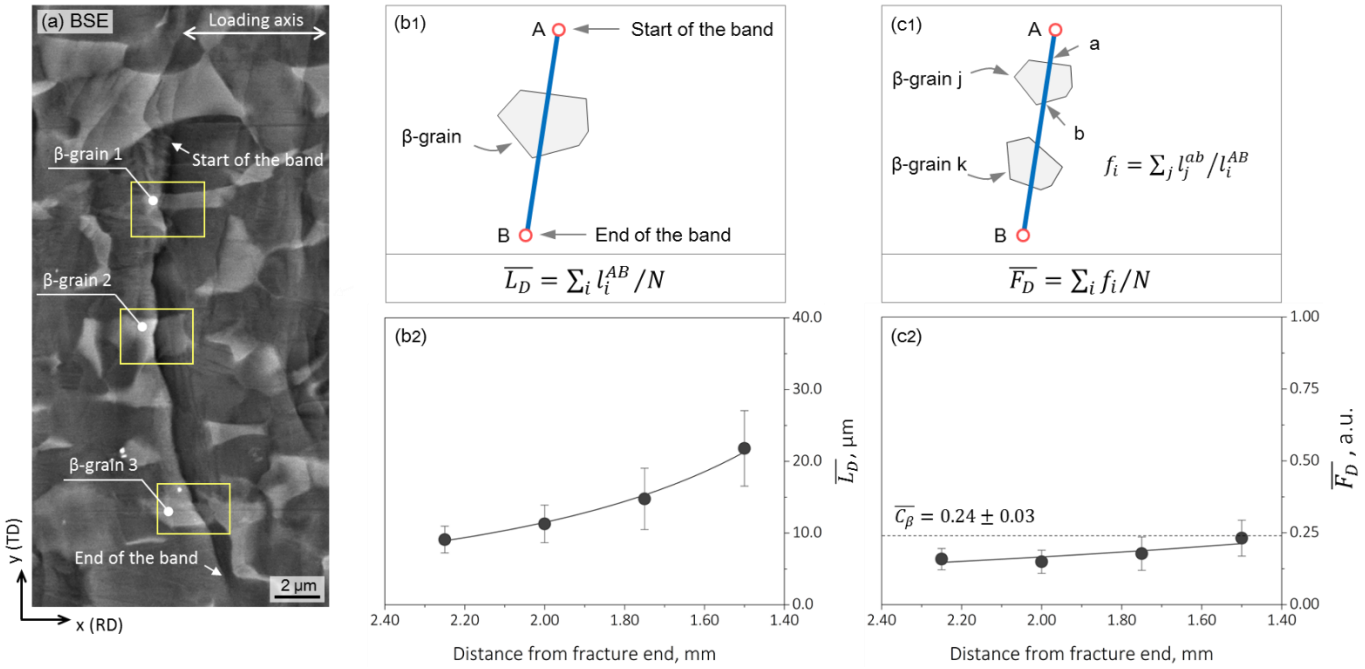

Fig. 7 | Quantitative assessments of strain localization band propagation: *(a) BSE micrograph showing the development of an individual strain localization band segmenting multiple β-grains; (b1) and (c1) schematics revealing the quantification parameter* $\overline{L_D}$ *and* $\overline{F_D}$*; (b2) and (c2) evolution of* $\overline{L_D}$ *and* $\overline{F_D}$ *with respect to the distance from fracture end. Error bars in (b2) and (c2) are standard deviations.*

While the foregoing analyses and discussion focus on the operative slip mechanisms within the strain localization region, it should be noted from a logical perspective that these results only assess the "*necessity*" for strain localization. That being said, given the fact that in the surveyed strain localization regions, prismatic ⟨**a**⟩ slip is predominant and its transfer into the β-phase is smooth ("*necessity*"), it is not guaranteed that every prismatic ⟨**a**⟩ slip and thus its transfer will eventually lead to strain localization ("*sufficiency*"). Direct justification of the "*sufficiency*" via the current experimental techniques may not be feasible, since it requires accurate identification and comparison between the portions of prismatic ⟨**a**⟩ slip and hence its transfer that accommodate homogenous plastic strain versus those leading to heterogeneous plastic strain. More recent coupled DDD-CPFEM simulation (Waheed et al., 2019; Yilun Xu et al., 2020) might exhibit the potential to enable a more comprehensive "*sufficiency*" justification. In an experimental viewpoint, however, some indirect investigations may still possible: if prismatic ⟨**a**⟩ slip activation and hence its transfer can intensify heterogeneous plastic strain development, it should be anticipated that the development of these long-range strain localization band is not accompanied by an eminent local hardening response. In other words, if the proposed "*necessity*" argumentation is completely lack of "*sufficiency*", the prismatic ⟨**a**⟩ slip activation and its transfer will immediately give rise to significant local strain hardening that brings about plastic strain delocalization and homogenization (Wu and Fan, 2020). This hypothesis enables the design of a quasi-in-situ experiment for verification, which involves nano hardness comparison between the regions with and without strain localization bands. The following Fig. 8 (a) reveals the region subjected to SEM-based nano-indentation experiment. It can be seen that the nano hardness values (Fig. 8 (c)) measured from the on-band region (pink dots), although exhibiting larger statistical scattering (3.22 ±0.31 GPa), are systematically lower than the region where no evident strain localization bands (blue dots) appear on the surface (3.82 ±0.17 GPa and 3.99 ±0.11 GPa). This kind of trend, although seemingly in accord with the hypothesis, requires

further explorations. One major reason is because the surface roughness change due to the strain localization band development may also affect the nano hardness measurement. To better quantify, cyclic nano-indentation was further performed, using the continuous stiffness mode so as to clarify the effect of surface roughness change. Compatible with the monolithic nano-indentation test (Fig. 8 (b)), consistently lower nano hardness values (although larger statistical scattering) present in the on-band region. Power function regression assessments reveal the nano hardness-indentation depth dependency approximately follows: $H = 3.318 + 0.0466d^{0.711}$ for the off-band region (Fig. 8 (d1)), and $H = 2.592 + 0.0355d^{0.817}$ for the on-band region (Fig. 8 (d2)). These two sets of independent measurements are therefore suggestive that the activation of prismatic slip and hence its propagation by smooth slip transfer is *at least not* bringing about an eminent local hardening effect, which indirectly supports its correlation with the development of strain localization in terms of the "*sufficiency*" consideration. It should be finally noted that the present nano-indentation experiment is largely a surface technique, which cannot unambiguously resolve the spatial mechanical effect of the strain localization effect. As discussed in the earlier Sections, such limitations can be plausibly improved in future studies by integrating three-dimensional CPFEM simulation and full-field X-ray diffractometry.

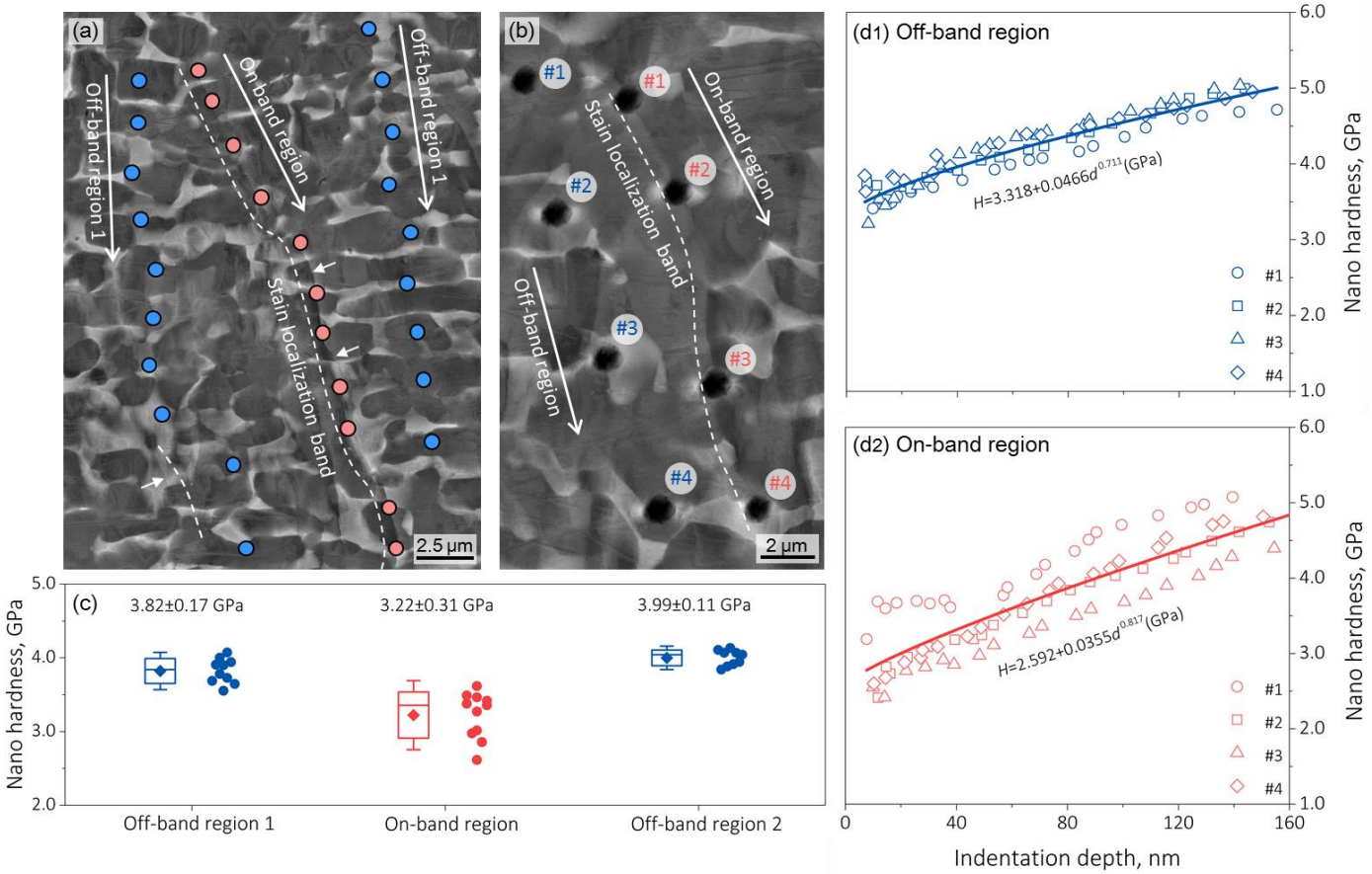

Fig. 8 | Nano-mechanical investigation of the strain localization behavior: *(a) and (b) BSE micrographs for the selected areas subjected to monolithic and cyclic nano-indentation test, which are ~2.00 mm from the fracture end; (c) box chart summarizing the nano hardness measurement for (a); (d1) and (d2) nano hardness versus indentation depth measured from cyclic nano-indentation test for (b).*

4.2 Evaluation of strain partitioning between α- and β-phases

In addition to texture, slip transferability, and strain localization inception elaborated in the previous discussion, intrinsic mechanical contrast between α- and β-phases also yields an important contribution to the heterogeneous plastic strain distribution. Especially, the phase-specific deformation response and thereby plastic strain partitioning amongst them critically affect the inception of local damage (Bieler et al., 2009; Latypov et al., 2016). However, the presence of the long-range strain localization bands (Fig. 3 (e)-(h)) retards the classical strain partitioning assessment route that based on point-wise sampling and arithmetic averaging (Dutta et al., 2019; Tasan et al., 2014a; Wang et al., 2017). Furthermore, strain heterogeneity description in these charts, although embedded in the prominent standard deviation, is often less informative and omitted for the corresponding analyses. To enable more reliable data representation and to also incorporate both strain partitioning and distribution quantification, the experimentally measured local strain profiles (Fig. 3 (a)-(h)) were subjected to lognormal regression analyses:

$$\xi(x) = \frac{1}{wx\sqrt{2\pi}} \exp\left\{-\frac{[\ln(x/x_c)]^2}{2w^2}\right\} \tag{9}$$

which has been recently reported as a phenomenologically universal feature for plastic strain distribution at a suitable statistical length-scale (Tang et al., 2020). In Eq. (9), $\xi(x)$, w, and x_c respectively denote the strain frequency (namely, the probability density) at a local plastic value of x, the multiplicative standard deviation, and the strain median. In the analyses onwards, the x_c values determined from the regression analyses are exploited as the representative local strains for targeted microstructural constituents, and the FWHM of $\xi(x)$ is employed to quantify the heterogeneity of strain distribution.

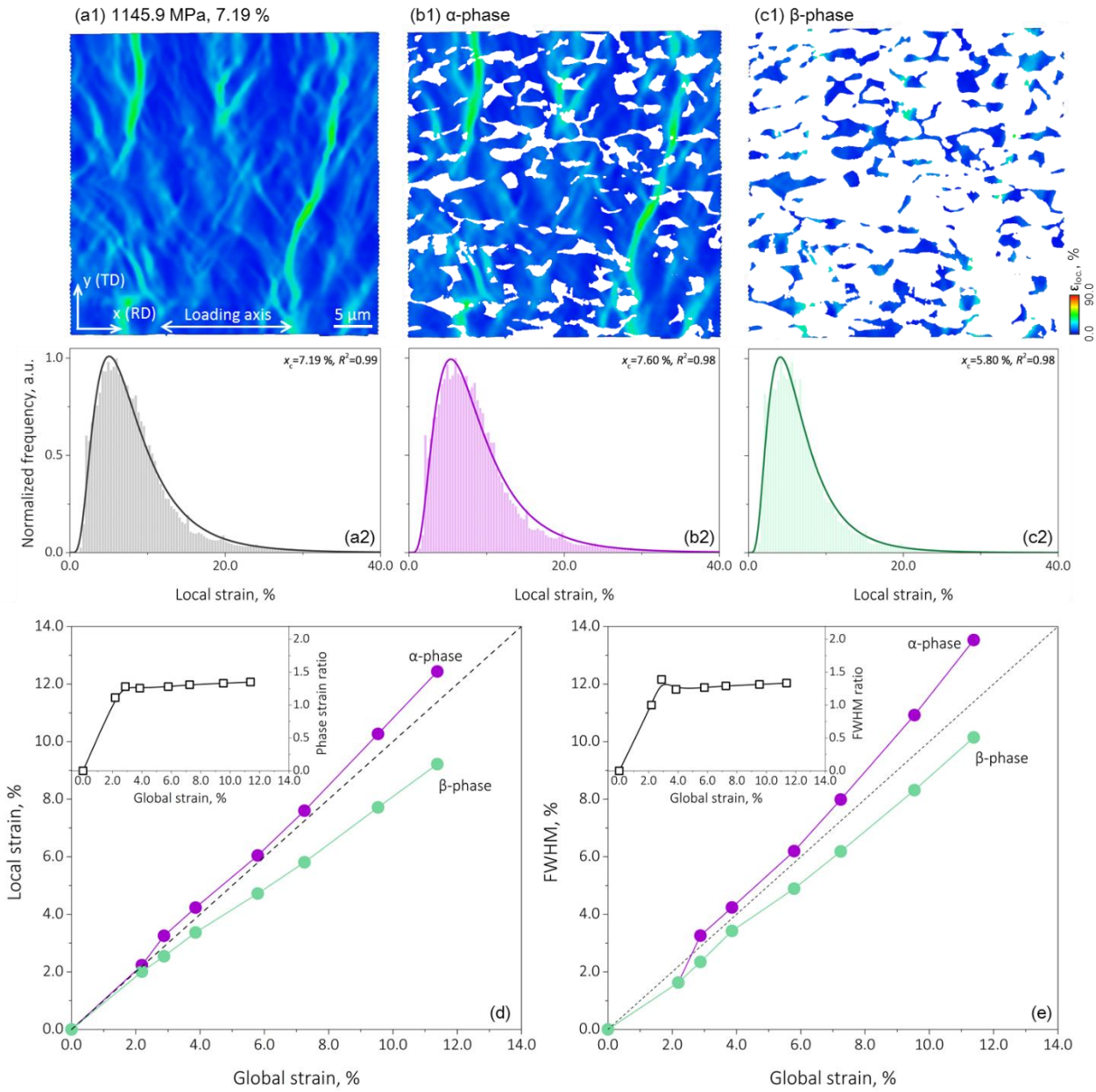

Fig. 9 | Statistical assessment of strain partitioning trend between α- and β- phases: *(a1)-(c1) exemplary strain maps subjected to the regression analysis; (a2)-(c2) lognormal regression analyses for the corresponding strain maps; (d) strain partitioning chart with inset showing the evolution of phase strain ratio; (e) phase strain heterogeneity evolution chart with inset displaying the resultant FWHM ratio. Plastic strain distribution charts for α- and β-phases were acquired by segmenting the original strain map using the in-beam BSE contrast, which intends to minimize the amount of data manipulation. Supplementary Fig. S5 reveals a detailed validation considering the phase boundary effect.*

Fig. 9 demonstrates the exemplary overall strain map acquired at a global deformation level of ~7.19% (engineering stress level: 1145.9 MPa) (Fig. 9 (a1)) as well as the partitioned strain maps for α- (Fig. 9 (b1)) and β-phases (Fig. 9 (c1)), with the associated regression analysis charts appended at the bottom (Fig. 9 (a2)-(c2)). At the global strain level of ~7.19%, it is recognized that the α- and β-phases respectively accommodate ~7.60% and 5.80% plastic strains, with the corresponding Pearson correlation coefficients (R^2) both approaching 0.98, which confirms the validity of the applied statistical length-scale. Following this approach, the strain partitioning chart as well as the corresponding heterogeneity evolution profile are calculated and presented in Fig. 9 (d) and (e). The α- and β-phases demonstrate an equal-strain accommodation until the global strain level reaches ~2.0%, beyond which evident strain partitioning starts to take place. While both the partitioned phase strains both

undergo approximately linear increase as a function of elevating global strain level, the α-phase bears a comparatively higher plastic strain and the β-phase, between which the difference approaches ~3.2% at a global strain level of ~12.4%. Such a partitioned phase strain difference is especially mild if compared with classical dual-phase steels, in the latter, ferrite and martensite can exhibit up to ~20% strain difference at a similar global strain level (Ososkov et al., 2007; Ryu et al., 2010; Tasan et al., 2014a; Wang et al., 2017). It is worthwhile noting that the present analyses acquire the plastic strain distribution charts for both phases by using the in-beam BSE contrast (Supplementary Fig. S1), which is intended to minimize the amount manipulation of the original dataset. However, as an inevitable shortcoming of the μ-DIC approach, strain data around plus (or minus) one strain window size (here is 20 pixel, in equivalent ~200 nm) of the phase boundary may comprise of contribution of both α- and β-phases. To ensure that this intrinsic ambiguity is not affecting the general conclusion drawn here, in Supplementary Fig. S5, a comparison is demonstrated for Fig. 9 (d) determined by excluding one strain window size of data points for both phases. It is confirmed that such potential artifacts in the current μ-DIC measurement is subtle, only creating ~0.2 % absolute difference in the local strain value at the highest deformation level. A more quantitative discussion is detailed next, based on nano-indentation investigations of the individual phase properties. Another interesting latent feature captured by Fig. 9 (d) lies in the evolution trend of the partitioned phase strain ratio between α- and β-phases (inset of Fig. 9(d)), which first undergoes a linear increase to 1.1 then reveals an asymptotic incrementation up to 1.35. This sort of character is also revealed in the FWHM ratio evolution of the strain distribution in α- and β-phases (inset of Fig. 9 (e)). Although the physical foundations for such a statistically convergent response still require further exploration, its evolutionary feature does suggest the phenomenological stabilization of plastic strain partition between microstructural constituents. From the plastic strain heterogeneity evolution perspective (Fig. 9 (e)), it is in accord with the mechanistic discussion in Section 4.1 that the FWHM of the α-phase strain yields higher values that that of the β-phase strain with global strain level greater than ~2.0%, signifying the stronger localization tendency.

Similar to dual-phase steels, strain partitioning in (α+β) titanium alloys is also affected by various factors, typically including individual phase strength, length scale, and volume fraction of the presenting phases, and crystallographic variants distribution in the transformed β-region. However, the following two microstructural characteristics of the present alloys steer the attention more towards phase strength contrast: first, less distinctive difference exists in the grain size and morphology of the α- and β-phases, and their distribution does not display eminent spatial inhomogeneity; second, transformed β-region, an aggregation of secondary α-phase and retained β-phase, is completely absent. Fig. 10 (a) presents the nanohardness distribution throughout a representative region of the microstructure. With the aid of EBSD measurement, these 144 nanoindents are categorized into four sub-groups based on their spatial positions (Fig. 10 (b)): (1) at α-phase interior; (2) at β-phase interior; (3) at α-phase grain boundary; and (4) at α/β PB. The position of each nano indent is identified by the corresponding EBSD phase map with a scan step of 0.1 μm. Amongst them, the nano hardness values of α- and β-phases respectively achieve 4.48±0.25 and 4.69±0.17 GPa (nano hardness ratio ~0.96) which are arithmetically averaged from 27 and 18 measurements. The difference in

nanohardness between the present α- and β-phases is evidently moderate if compared with that between ferrite and martensite in dual-phase steels, the latter, according to numerous literature (Baltazar Hernandez et al., 2010; Delinc éet al., 2006; Mazaheri et al., 2015; Morsdorf et al., 2015; Taylor et al., 2014) can achieve up to 6 GPa discrepancy. Such a comparatively moderate phase strength difference in the present alloy in turn results in the milder strain partitioning characteristic between α- and β-phases (Fig. 10 (d)). The higher plastic strain partitioned by the α-phase is therefore largely ascribed to its inferior strength and thereby yield resistance, regarding which the phase property is next semi-quantitatively evaluated using the reverse algorithm (Dao et al., 2001; Gouldstone et al., 2007). The adopted reverse analysis presume α- and β-phases both exhibit Hookian responses in the elastic realm and power-law hardening in the plastic realm (calculation details are summarized in Supplementary Note. 1). The derived compressive stress-strain curves for representative nanoindents on α- and β-phases (Fig. 10 (c) and (d)) are presented in Fig. 10 (e) with the corresponding analytical results summarized in Eqs. (10) and (11):

$$\sigma_\alpha = \begin{cases} 134.21\varepsilon_e \\ 2.26\left(1 + 59.31\varepsilon_p\right)^{0.217} \end{cases} \tag{10}$$

$$\sigma_\beta = \begin{cases} 112.13\varepsilon_e \\ 2.76\left(1 + 40.57\varepsilon_p\right)^{0.188} \end{cases} \tag{11}$$

In accord with the nanohardness trends, the α-phase exhibits a comparatively lower derived yield strength than the β-phase (2.26 versus 2.76 GPa), although the derived strain hardenability yields a subtle discrepancy (strain hardening exponent: 0.217 versus 0.188). These quantitative analyses lead to the following mechanistic insights into the foregoing strain partitioning results (Fig. 8 (d) and (e)): first, because of its inferior plastic resistance and the higher elastic modulus, yielding tends to initiate in the α-phase prior to the β-phase at a comparatively lower global plastic strain level. This in turn results in the higher plastic strain partitioning in the α-phase as observed in Fig. 8 (d); second, plastic yielding is postponed in the β-phase due to its higher derived yield strength, however, once it also undergoes plastic deformation, the resultant strain hardenability is seemingly close to the α-phase. Such a feature tends to proportionally intensify the strain partitioning characteristic, plausibly giving rise to the asymptotic evolution of the phase strain and FWHM ratios (insets of Fig. 8 (d) and (e)). It shall be noted that the higher strength revealed in the β-phase could be intrinsically owing to the dissolution of Fe (see Fig. 1 (d)), whose enrichment in the β-phase has been documented to render a salient solid solution strengthening effect (Ehtemam-Haghighi et al., 2017; Min et al., 2012). As a final remark, although the present investigation for strain partitioning mostly focuses on the effect of mechanical responses of the presenting phases, the microstructural inhomogeneity may also play a role in affecting the strain portioning characteristics. In fact, as revealed in the quantitative analyses for the penetrative nature of the strain localization band (Fig. 7), eminent strain localization could occur in regions where the local β-phase content is rather lean, also leading to a higher partitioned plastic strain in the α-phase. A potential proposition for future study is therefore to more accurately compare the effects of microstructural inhomogeneity and invaluable phase property distinctions on the resultant

strain partitioning characteristics.

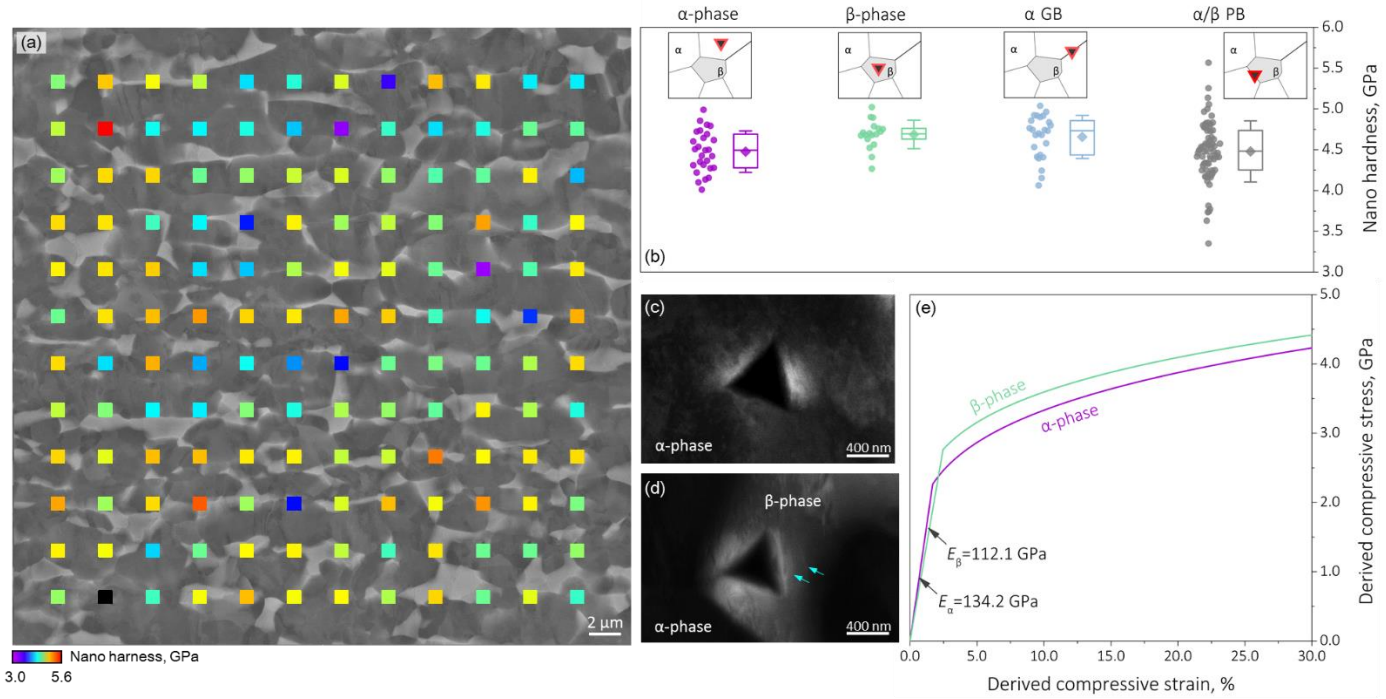

Fig. 10 | Nano mechanical exploration of individual phase properties: *(a) color map showing the nanohardness distribution in the elected area of interest; (b) box chart for the nanohardness values at different microstructural sites; (c) and (d) two representative nanoindents that are subjected to further quantification (cyan arrows highlight the presence of slip steps); (e) derived compressive stress-strain response for the α- and β-phases. Abbreviations adopted: grain boundary (GB), and phase boundary (PB).*

4.3 Damage mechanisms and deformation features at post-uniform elongation region

Although the governing damage microincidents in (α+β) titanium alloys can exhibit salient microstructural dependency, the α/β phase boundary decohesion mechanism (originating from plastic strain incompatibility) has been widely accepted as the critical cracking module (Lefranc et al., 2008; Shao et al., 2013; Wei et al., 2019a; X. Zhang et al., 2018). Often, principal cracks in the foregoing alloys tend to develop evident spatial alignments compatible with the geometry of α/β PBs, however, fracture morphology taken at the RD×TD surface clearly reveals the presence of vertical cracks that are largely independent of α/β PBs (Fig. 11 (a)). A closer comparison between Fig. 11 (a) and the previous in-situ μ-DIC results in Fig. 3 suggest the spatial and length-scale compatibility between the pronounced strain localization bands and the observed surface crack. It would be expected that if all the matured strain localization bands are acting as the governing damage micro-mechanisms, the fracture surface will therefore exhibit evident brittle-like features (Abuzaid et al., 2013; Dao and Lit, 2001; Wei et al., 2019b). Interestingly, fractography acquired for the TD×ND surface (Fig. 11 (b)) suggests that while some local regions do exhibit dimple-free bands (Fig. 11 (c1) and (c2)) with tens of micrometer in their lengths that are parallel to the TD, majority of the fracture surface consists of small dimples, which are typical failure features of relatively homogeneous micro-void nucleation, growth, and coalescence. The distinctions observed from RD×TD and TD×ND surfaces have two implications: first, while strain localization region can initiate long-range cracking on the surface, these cracks may not necessarily penetrate into the

bulk and their depth are rather shallow; and second, micro-void involved damage processes seem to reveal the more predominant role in the eventual fracture of the present alloy.

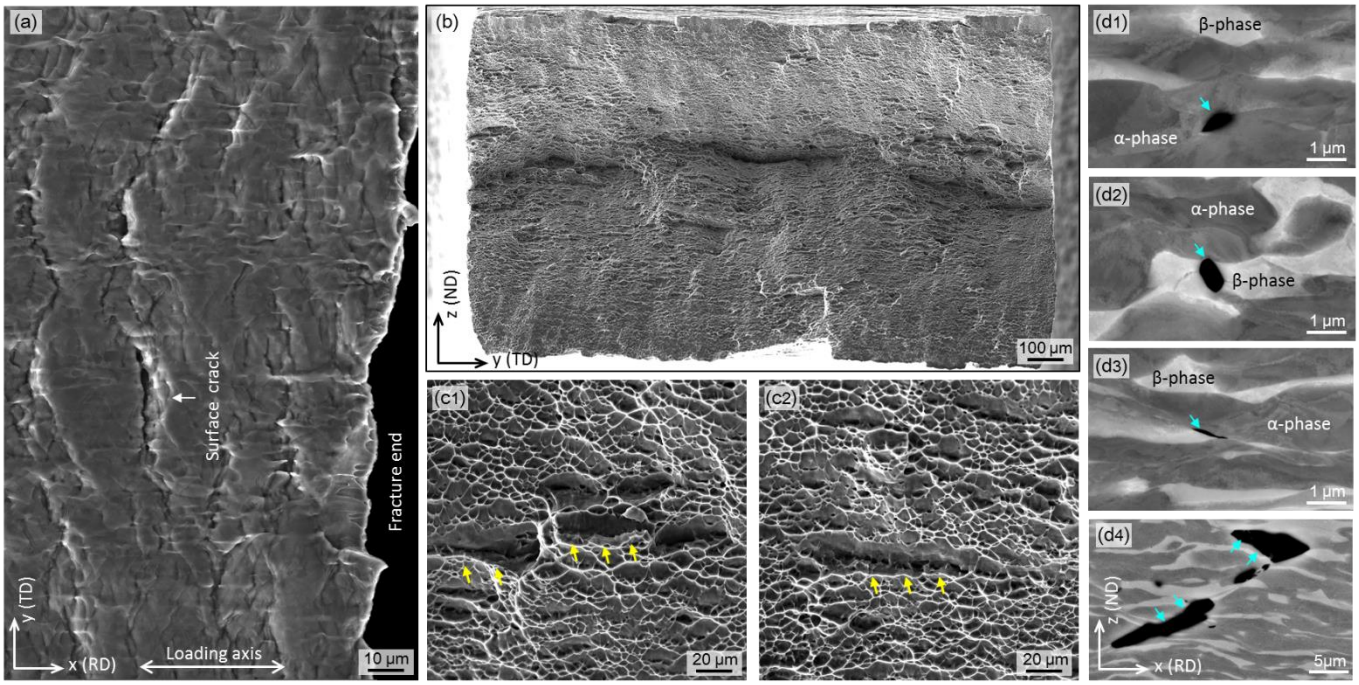

Fig. 11 | Damage characteristics of the present alloy after uniaxial tensile testing: *(a) morphology of the principal penetrative cracks at the RD×TD surface; (b) fractography take at the TD×ND surface; (c1)-(c2) representative local dimple-free zones at the fracture surface; (d1)-(d4) categorization of the damage micro-incidents, from top to bottom: α-phase damage, β-phase damage, α/β PB damage, and penetrative cracking whose origin cannot be unambiguously identified.*

To further investigate the predominant damage process, micrographs (RD×TD surface) shown in Fig. 11 (d1)-(d4) categorize the representative damage microincidents into α-phase damage (Fig. 11 (d1)), β-phase damage (Fig. 11 (d2)), α/β PB damage (Fig. 11 (d3)), and penetrative cracking (Fig. 11 (d4)) whose origin cannot be unambiguously identified by using the current post-mortem experimental technique. Detailed quantifications including the evolution of the number of damage incident, damage area fraction, and average damage size with respect to the local strain level are shown in Fig. 12. Similar to the previous reports, most of the damage incidents indeed nucleate at the α/β PB, with its number increasing from 61 to 174 as the local strain increases from 27.4 % to ~42.5 % (Fig. 12 (a)). In terms of the damage area fraction (Fig. 12 (b)) as well as the averaged damage size (Fig. 12 (c)), damage incidents along the α/β PB are also more dominant than α- or β-phase interior throughout the survey local strain levels. Another interesting phenomenon demonstrated by Fig. 12 is that micro-voids do nucleate in both α- and β-phases, and particularly, a higher number of micro-voids in the α-phase is revealed in Fig. 12 (a). This kind of results is slightly different from conventional understandings, because the β-phase in titanium alloys is often believed to exhibit the lower strength than α-phase and should be more prone to micro-void nucleation. However, two microstructural features of the present alloy could be plausibly explain such distinctions: intrinsically, as supported by the nano hardness measurements the β-phase of the present alloy is revealing a higher strength than the α-phase: the corresponding nano hardness values are 4.69±0.17 GPa (β-phase) and 4.48±0.25 GPa (α-phase). This sort of intrinsic difference could be due to the Fe-rich nature of

the β-phase (Fig. 1 (d)), which has been reported to render an evident solid solution strengthening effect in titanium alloys (Ehtemam-Haghighi et al., 2017; Min et al., 2012). Extrinsically, the combination of the loading direction along with the texture property of the present alloy may also play a role. The strong rolling direction developed in the α-phase (Fig. 1 (c)) brings about the fact that uniaxial tensile deformation along the RD direction is seemingly closer to the crystallographic "*soft*" axis of the α-phase. A combination of both the intrinsic properties and the extrinsic testing condition of the present alloy could plausibly account for the fact that more micro-voids develop within the α-phase than the β-phase. It should be again highlighted that the present damage mechanism assessment is based on two-dimensional Sections of the microstructure. A more comprehensive evaluation could be accomplished in future study by characterizing the crystallographic dependency of the damage incidents by three-dimensional stereological reconstruction approaches. Still, a qualitative exploration might be made by using the two-dimensional slip trace information (Table 1.). Supplementary Fig. S6 and Table S2 summarize the calculation results of the intersection angles between activated slip planes within the strain localization bands and the specimen's top surface. It is recognized that although the long-range strain localization bands are nearly perpendicular to the loading axis, the corresponding intersection angles are rather close to 45 degrees. Such a trend is in line with the Schmid factor analysis presented in Section 4.1, which highlights the importance of shear stress. As a result of this, it could be deduced that the three-dimensional orientation of the strain-localization-induced cracks will closely follow the orientation of the slip planes activated within them.

The distinctive role between the strain localization-induced surface cracking and the micro-void nucleation-growth driven cracking in the eventual failure process of the present alloy still leads to a fundamental proposition that is worth discussing, that is the interplay between macroscopic stress state and the development of surface crack. Classical theory developed for micro-void nucleation highlights the importance of stress triaxiality (Johnson and Cook, 1985; McClintock, 1964), which states the micro-void nucleation and growth tendency is positively related with the relative degree of hydrostatic stress in a given stress state. The microscopic validity of this theory implies that given the macroscopic near-plane stress condition of the thin sheet specimen under uniaxial tension loading, localized shear event tends to mitigate stress triaxiality, which hinders the nucleation and growth of micro-voids. However, more recent in-situ deformation studies of ferrite-martensite dual-phase steels do highlight that if the presenting phases are exhibiting a significant difference in their strengths, the local stress state can be highly deviated from the macroscopic condition, which as a result brings about micro-voids nucleation and growth at the surface (Avramovic-Cingara et al., 2009; Lai et al., 2015; Pütz et al., 2020; Toda et al., 2017).

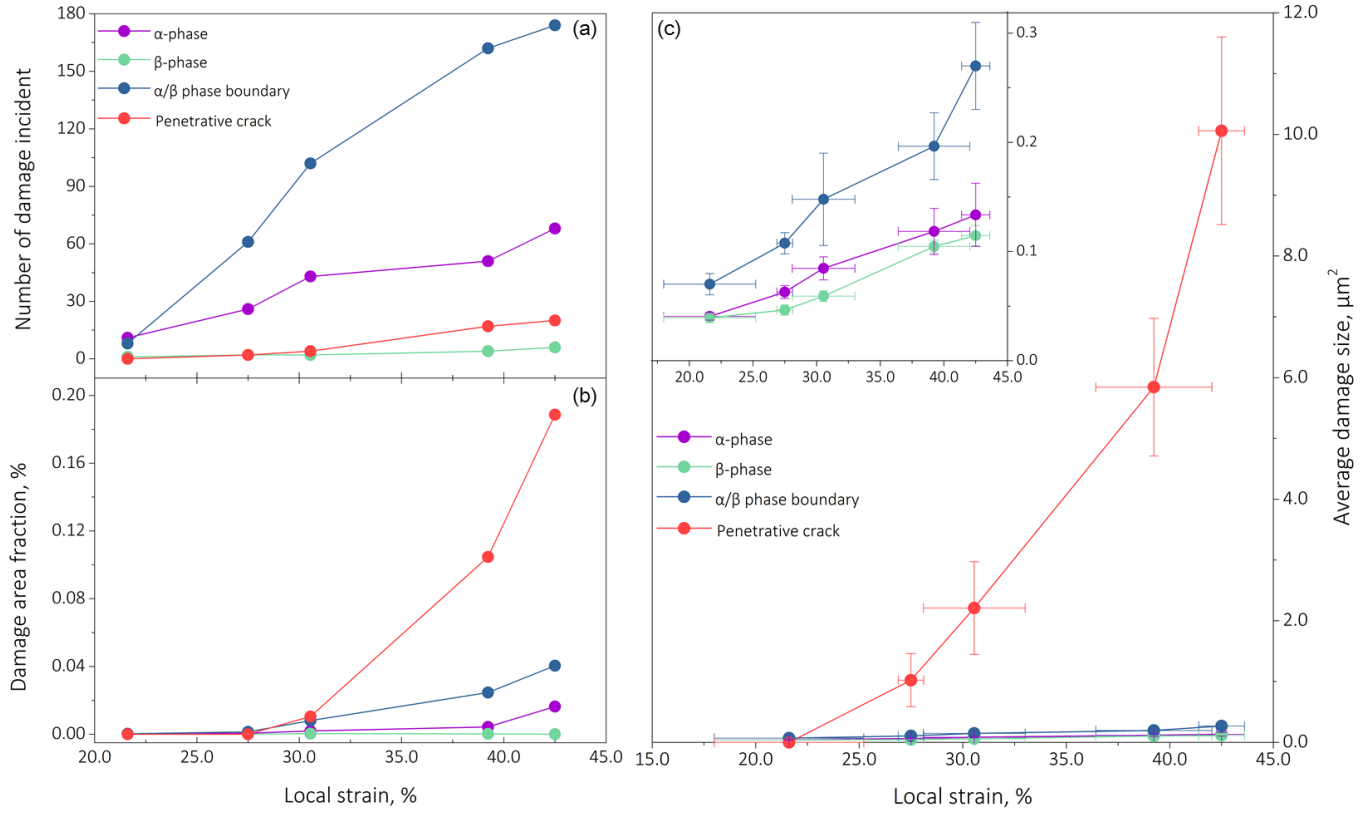

Fig. 12 | Quantitative post-mortem damage evolution charts with respect to increasing local strain level*: (a) number of damage incident; (b) damage area fraction; (c) average damage size.*

To further explore, a "stitched μ-DIC" strategy was exploited to probe and compare deformation features close to various damage incidents, intentionally in the post-uniform elongation region. Fig. 13 (a) shows the microstructural morphology of the present alloy at a pre-strain level of ~11.4 %, whose surface topography induced by plastic deformation has been removed following the experimental procedure detailed in Section 2.2. Higher-magnification BSE micrographs reveal the presence of damage incidents nucleating in the α-phase interior (Fig. 12 (a1)), at α/β PB (Fig. 13 (a2)), and in the β-phase interior (Fig. 13 (a3)), of which the sizes only reach a few micrometers. When again being subjected to plastic straining, the representative μ-DIC map (Fig. 13(b)) elaborates the following three major features: (1) the foregoing three prior damage incidents reveal a negligible increase in their dimensions and no evident coalescence is observed (Fig. 12 (a1)-(a3) versus (b1)-(b3)); (2) local strain levels developed around these incidents are rather homogenous with subtle localization tendency presented (Fig. 13 (b1)-(b3)); and (3) similar to the μ-DIC results discussed in Fig. 3 and Section 4.1, long-range strain localization bands that are nearly vertical to the loading direction reoccur, showing a characteristic peak local strain level close to ~15.0 %. By comparing the local strain levels at the vicinity of the prior damage incidents and a typical strain localization band, almost an order of magnitude higher local strain is developed in the latter, at only ~1.9 % global strain level. These results are informative that although plastic strain indeed exhibits a clear partitioned trend between α- and β-phases, the phase strength difference (implied by the nano hardness values) is not high enough to significantly deviate the local stress-state and enable discernable micro-void growth as observed in dual-phase steels. It is therefore suggested that strain localization is the predominant source for surface cracking, although in the bulk of the present alloy relatively homogenous micro-void nucleation, growth, and

coalescence is the major cause for final ductile fracture.

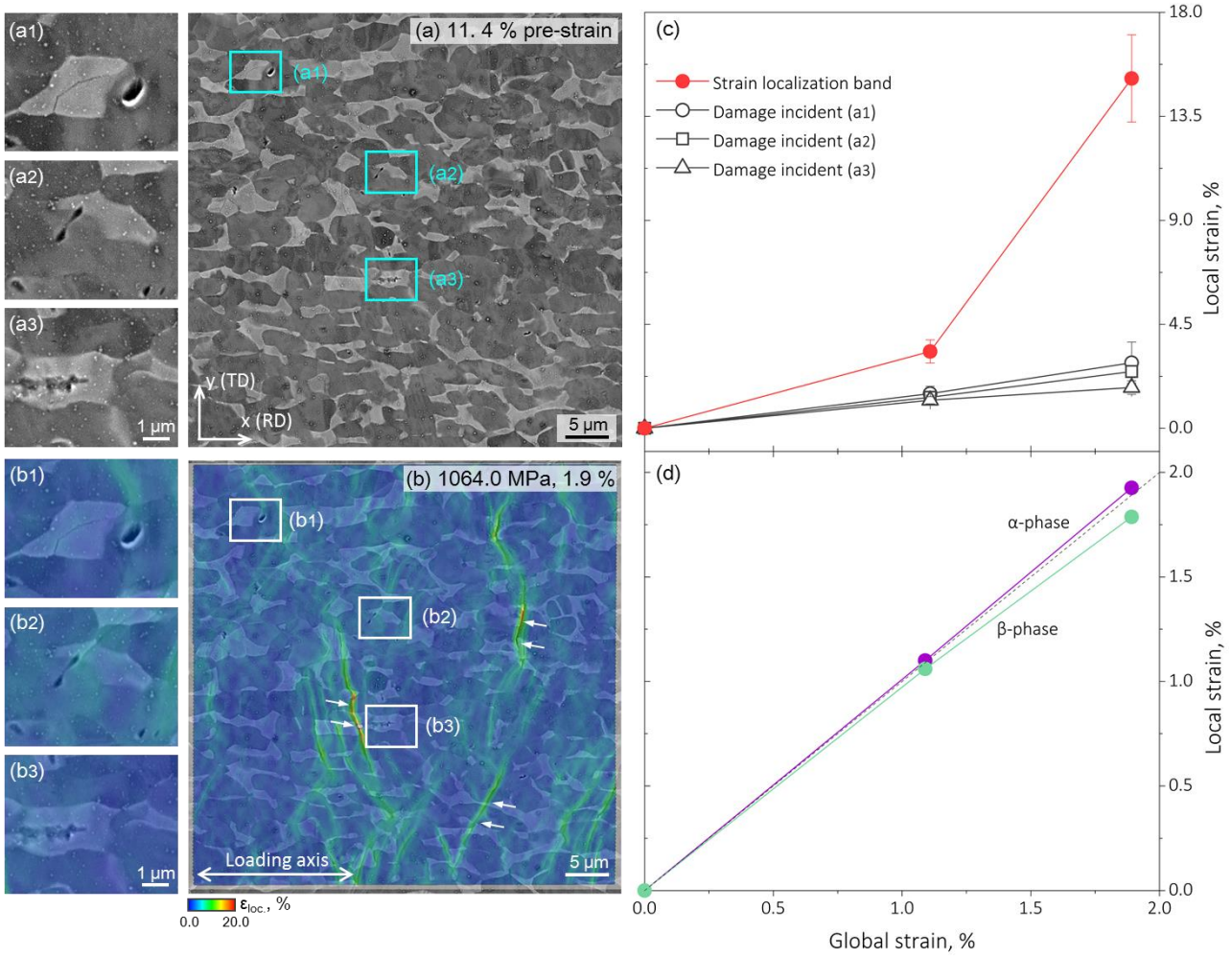

Fig. 13 | *In-situ "stitched μ-DIC" analyses for damage mechanisms validation: (a) the selected area of interest after ~11.4 % pre-strain; (a1)-(a3) magnified micrographs for representative damage incidents, top to bottom: α-phase damage, α/β PB damage, and β-phase damage; (b) local strain distribution at ~1.9 % and 1064.0 MPa deformation level; (b1)-(b3) magnified strain maps correspond to (a1)-(a3); (c) comparison between local strain evolution at various microstructural sites (point-wise data acquisition is applied, and local strain values for 5 vicinal facets are averaged for each data point); (d) statistical assessment of strain partitioning at the post-uniform elongation region.*

5. Conclusions

By integrating in-situ SEM/EBSD/μ-DIC experimentations, the present work examines the heterogeneous deformation characteristics in a Ti-Al-V-Fe (α+β) alloy, with specific aims to clarify the role of the operating deformation mechanisms in strain localization and partitioning and thereby understand their relation with damage inception. Major findings are summarized as follows:

(1) Microstructure-level deformation features in the present Ti-Al-V-Fe (α+β) alloy are characterized by the pronounced long-range strain localization bands that initiate in the α-phase, barely impeded by the presence of GBs or PBs. Crystallographic calculations verify that texture-facilitated extensive prismatic ⟨**a**⟩ slip and hence its smooth transfer into the β-phase are the

predominant deformation micro-mechanisms within these strain localization bands

(2) Statistical assessment of the μ-DIC results elaborates the moderate strain partitioning response between α- and β-phases as well as the asymptotic evolution trend of the resultant partitioned phase strain ratio. Such characteristics are owing to the mild strength difference between the presenting phases together with the similar strain hardenability, which is implied by the nano indentation measurement. These observations also compatible with the crystallographic assessment, suggesting the near-optimal slip transferability across α/β PBs;

(3) Damage analyses carried out along the surface, fracture surface, and fracture cross-section show that although the strain localization region is noticeably associated with the development of surface cracks, they are rather shallow in depth and do not exhibit a discernable penetrative characteristics. Final fracture of the present alloy is mostly governed by the nucleation, growth, and coalescence of micro-voids. Further quantitative analyses also confirm the higher amount of micro-voids nucleate within the α-phase, which is possibly ascribed to its lower strength along with the combination of loading condition and texture.

Acknowledgments

The authors express their sincere gratitude to the reviewers for their tremendous effort in providing constrictive feedback to this manuscript. S.L.W. and C.C.T. were financially supported by Allegheny Technologies Incorporated (ATI), Natrona Heights, PA, USA. Synchrotron X-ray radiation source benefits from beamline 11ID-C at the Argonne National Laboratory, Chicago, USA (with enthusiastic support from Drs. Yang Ren and Pengyue Gao). S.L.W. thanks Dr. Shao-Shi Rui for the critical discussion about crystal plasticity.

Author contributions

Shaolou Wei: conceptualization, experimental investigations, programing, theoretical calculations, formal analysis, and writing-original draft. **Jinwoo Kim**: experimental investigations and discussion. **Cemal Cem Tasan**: conceptualization, formal analysis, writing-review & editing, and supervision. All authors discussed and approved the final version of the manuscript.

Declaration of competing interest

The authors declare that they have no known competing financial interests or personal relationships that could have appeared to influence the work reported in this manuscript.

References

Abdolvand, H., Wright, J., Wilkinson, A.J., 2018. Strong grain neighbour effects in polycrystals. Nat. Commun. https://doi.org/10.1038/s41467-017-02213-9

Abuzaid, W., Sehitoglu, H., Lambros, J., 2013. Plastic strain localization and fatigue micro-crack formation in Hastelloy X. Mater.

Sci. Eng. A. https://doi.org/10.1016/j.msea.2012.10.072

Ahmad, R., Wu, Z., Curtin, W.A., 2020. Analysis of double cross-slip of pyramidal I 〈c+a〉 screw dislocations and implications for ductility in Mg alloys. Acta Mater. https://doi.org/10.1016/j.actamat.2019.10.053

Anderson, P.M., Hirth, J.P., Lothe, J., 2017. Theory of dislocations 3rd Edition.

Arul Kumar, M., Beyerlein, I.J., McCabe, R.J., Tomé, C.N., 2016. Grain neighbour effects on twin transmission in hexagonal close-packed materials. Nat. Commun. https://doi.org/10.1038/ncomms13826

ASTM, 2013. ASTM E112-13: Standard test methods for determining average grain size. ASTM Int.

Avramovic-Cingara, G., Ososkov, Y., Jain, M.K., Wilkinson, D.S., 2009. Effect of martensite distribution on damage behaviour in DP600 dual phase steels. Mater. Sci. Eng. A 516, 7–16. https://doi.org/10.1016/j.msea.2009.03.055

Baltazar Hernandez, V.H., Panda, S.K., Kuntz, M.L., Zhou, Y., 2010. Nanoindentation and microstructure analysis of resistance spot welded dual phase steel. Mater. Lett. https://doi.org/10.1016/j.matlet.2009.10.040

Banerjee, D., Williams, J.C., 2013. Perspectives on titanium science and technology. Acta Mater. https://doi.org/10.1016/j.actamat.2012.10.043

Barbe, F., Quey, R., Musienko, A., Cailletaud, G., 2009. Three-dimensional characterization of strain localization bands in high-resolution elastoplastic polycrystals. Mech. Res. Commun. https://doi.org/10.1016/j.mechrescom.2009.06.002

Baudoin, P., Hama, T., Takuda, H., 2019. Influence of critical resolved shear stress ratios on the response of a commercially pure titanium oligocrystal: Crystal plasticity simulations and experiment. Int. J. Plast. https://doi.org/10.1016/j.ijplas.2018.11.013

Bayerschen, E., McBride, A.T., Reddy, B.D., Böhlke, T., 2016. Review on slip transmission criteria in experiments and crystal plasticity models. J. Mater. Sci. https://doi.org/10.1007/s10853-015-9553-4

Bieler, T.R., Alizadeh, R., Peña-Ortega, M., Llorca, J., 2019. An analysis of (the lack of) slip transfer between near-cube oriented grains in pure Al. Int. J. Plast. https://doi.org/10.1016/j.ijplas.2019.02.014

Bieler, T.R., Eisenlohr, P., Roters, F., Kumar, D., Mason, D.E., Crimp, M.A., Raabe, D., 2009. The role of heterogeneous deformation on damage nucleation at grain boundaries in single phase metals. Int. J. Plast. https://doi.org/10.1016/j.ijplas.2008.09.002

Bieler, T.R., Eisenlohr, P., Zhang, C., Phukan, H.J., Crimp, M.A., 2014. Grain boundaries and interfaces in slip transfer. Curr. Opin. Solid State Mater. Sci. https://doi.org/10.1016/j.cossms.2014.05.003

Birosca, S., Di Gioacchino, F., Stekovic, S., Hardy, M., 2014. A quantitative approach to studying the effect of local texture and heterogeneous plastic strain on the deformation micromechanism in RR1000 nickel-based superalloy. Acta Mater. https://doi.org/10.1016/j.actamat.2014.04.039

Bormann, F., Peerlings, R.H.J., Geers, M.G.D., Svendsen, B., 2019. A computational approach towards modelling dislocation transmission across phase boundaries. Philos. Mag. https://doi.org/10.1080/14786435.2019.1612961

Bridier, F., Villechaise, P., Mendez, J., 2008. Slip and fatigue crack formation processes in an α/β titanium alloy in relation to crystallographic texture on different scales. Acta Mater. https://doi.org/10.1016/j.actamat.2008.04.036

Bunge, H.-J., 1982. Texture Analysis in Materials Science, Texture Analysis in Materials Science. https://doi.org/10.1016/c2013-0-11769-2

Cappola, J., Stinville, J.C., Charpagne, M.A., Callahan, P.G., Echlin, M.P., Pollock, T.M., Pilchak, A., Kasemer, M., 2021. On the Localization of Plastic Strain in Microtextured Regions of Ti-6Al-4V. Acta Mater. 204. https://doi.org/10.1016/j.actamat.2020.116492

Castany, P., Pettinari-Sturmel, F., Douin, J., Coujou, A., 2008. In situ transmission electron microscopy deformation of the titanium alloy Ti-6Al-4V: Interface behaviour. Mater. Sci. Eng. A. https://doi.org/10.1016/j.msea.2006.10.183

Cepeda-Jiménez, C.M., Molina-Aldareguia, J.M., Pérez-Prado, M.T., 2016. EBSD-Assisted Slip Trace Analysis During In Situ SEM Mechanical Testing: Application to Unravel Grain Size Effects on Plasticity of Pure Mg Polycrystals. JOM. https://doi.org/10.1007/s11837-015-1521-6

Chan, K.S., Koss, D.A., 1983. Deformation and fracture of strongly textured Ti alloy sheets in uniaxial tension. Metall. Trans. A. https://doi.org/10.1007/BF02664816

Charpagne, M.A., Stinville, J.C., Callahan, P.G., Texier, D., Chen, Z., Villechaise, P., Valle, V., Pollock, T.M., 2020. Automated and quantitative analysis of plastic strain localization via multi-modal data recombination. Mater. Charact. https://doi.org/10.1016/j.matchar.2020.110245

Chen, B., Jiang, J., Dunne, F.P.E., 2018. Is stored energy density the primary meso-scale mechanistic driver for fatigue crack

nucleation? Int. J. Plast. https://doi.org/10.1016/j.ijplas.2017.11.005

Cherukara, M.J., Pokharel, R., O'Leary, T.S., Baldwin, J.K., Maxey, E., Cha, W., Maser, J., Harder, R.J., Fensin, S.J., Sandberg, R.L., 2018. Three-dimensional X-ray diffraction imaging of dislocations in polycrystalline metals under tensile loading. Nat. Commun. https://doi.org/10.1038/s41467-018-06166-5

Chong, Y., Deng, G., Yi, J., Shibata, A., Tsuji, N., 2019. On the strain hardening abilities of α+β titanium alloys: The roles of strain partitioning and interface length density. J. Alloys Compd. https://doi.org/10.1016/j.jallcom.2019.152040

Chong, Y., Zheng, R., Deng, G., Shibata, A., Tsuji, N., 2020. Investigation on the Microstructure and Mechanical Properties of Ti-1.0Fe Alloy with Equiaxed α + β Microstructures. Metall. Mater. Trans. A Phys. Metall. Mater. Sci. 51, 2851–2862. https://doi.org/10.1007/s11661-020-05760-x

Cruzado, A., Lucarini, S., LLorca, J., Segurado, J., 2018. Microstructure-based fatigue life model of metallic alloys with bilinear Coffin-Manson behavior. Int. J. Fatigue. https://doi.org/10.1016/j.ijfatigue.2017.10.014

Cui, D., Zhang, Y., He, F., Ma, J., Zhang, K., Yang, Z., Li, J., Wang, Z., Kai, J. jung, Wang, J., Jun, F., 2021. Heterogeneous microstructure of the bonding zone and its dependence on preheating in hybrid manufactured Ti-6Al-4V. Mater. Res. Lett. 9, 422–428. https://doi.org/10.1080/21663831.2021.1958947

Dao, M., Chollacoop, N., Van Vliet, K.J., Venkatesh, T.A., Suresh, S., 2001. Computational modeling of the forward and reverse problems in instrumented sharp indentation. Acta Mater. https://doi.org/10.1016/S1359-6454(01)00295-6

Dao, M., Lit, M., 2001. A micromechanics study on strain-localization-induced fracture initiation in bending using crystal plasticity models. Philos. Mag. A Phys. Condens. Matter, Struct. Defects Mech. Prop. https://doi.org/10.1080/01418610108216649

Das, A., Tarafder, S., Sivaprasad, S., Chakrabarti, D., 2019. Influence of microstructure and strain rate on the strain partitioning behaviour of dual phase steels. Mater. Sci. Eng. A. https://doi.org/10.1016/j.msea.2019.03.084

Deka, D., Joseph, D.S., Ghosh, S., Mills, M.J., 2006. Crystal plasticity modeling of deformation and creep in polycrystalline Ti-6242. Metall. Mater. Trans. A Phys. Metall. Mater. Sci. https://doi.org/10.1007/s11661-006-0082-2

Delincé, M., Jacques, P.J., Pardoen, T., 2006. Separation of size-dependent strengthening contributions in fine-grained Dual Phase steels by nanoindentation. Acta Mater. https://doi.org/10.1016/j.actamat.2006.03.031

Dutta, A., Ponge, D., Sandlöbes, S., Raabe, D., 2019. Strain partitioning and strain localization in medium manganese steels measured by in situ microscopic digital image correlation. Materialia. https://doi.org/10.1016/j.mtla.2019.100252

Echlin, M.P., Stinville, J.C., Miller, V.M., Lenthe, W.C., Pollock, T.M., 2016. Incipient slip and long range plastic strain localization in microtextured Ti-6Al-4V titanium. Acta Mater. https://doi.org/10.1016/j.actamat.2016.04.057

Ehtemam-Haghighi, S., Cao, G., Zhang, L.C., 2017. Nanoindentation study of mechanical properties of Ti based alloys with Fe and Ta additions. J. Alloys Compd. https://doi.org/10.1016/j.jallcom.2016.09.123

Eshelby, J.D., Frank, F.C., Nabarro, F.R.N., 1951. XLI. The equilibrium of linear arrays of dislocations. London, Edinburgh, Dublin Philos. Mag. J. Sci. https://doi.org/10.1080/14786445108561060

Fan, X.G., Jiang, X.Q., Zeng, X., Shi, Y.G., Gao, P.F., Zhan, M., 2018. Modeling the anisotropy of hot plastic deformation of two-phase titanium alloys with a colony microstructure. Int. J. Plast. https://doi.org/10.1016/j.ijplas.2018.02.010

Fernández, A., Jérusalem, A., Gutiérrez-Urrutia, I., Pérez-Prado, M.T., 2013. Three-dimensional investigation of grain boundary-twin interactions in a Mg AZ31 alloy by electron backscatter diffraction and continuum modeling. Acta Mater. https://doi.org/10.1016/j.actamat.2013.09.005

Flipon, B., Keller, C., Quey, R., Barbe, F., 2020. A full-field crystal-plasticity analysis of bimodal polycrystals. Int. J. Solids Struct. https://doi.org/10.1016/j.ijsolstr.2019.02.005

Gil, F.J., Ginebra, M.P., Manero, J.M., Planell, J.A., 2001. Formation of α-Widmanstätten structure: Effects of grain size and cooling rate on the Widmanstätten morphologies and on the mechanical properties in Ti6Al4V alloy. J. Alloys Compd. https://doi.org/10.1016/S0925-8388(01)01571-7

Gilormini, P., Bacroix, B., Jonas, J.J., 1988. Theoretical analyses of 〈111〉 pencil glide in b.c.c. crystals. Acta Metall. https://doi.org/10.1016/0001-6160(88)90001-6

Gouldstone, A., Chollacoop, N., Dao, M., Li, J., Minor, A.M., Shen, Y.L., 2007. Indentation across size scales and disciplines: Recent developments in experimentation and modeling. Acta Mater. https://doi.org/10.1016/j.actamat.2006.08.044

Gurtin, M.E., 2008. A theory of grain boundaries that accounts automatically for grain misorientation and grain-boundary orientation. J. Mech. Phys. Solids. https://doi.org/10.1016/j.jmps.2007.05.002

Gurtin, M.E., Fried, E., Anand, L., 2010. The Mechanics and Thermodynamics of Continua, The Mechanics and Thermodynamics of Continua. https://doi.org/10.1017/cbo9780511762956

Hall E. O., 1951. The deformation and ageing of mild steel III Discussion of results. Proc. Phys. Soc. Sect. B 64, 747. https://doi.org/10.1088/0370-1301/64/9/303

Han, Q., Asgari, A., Hodgson, P.D., Stanford, N., 2014. Strain partitioning in dual-phase steels containing tempered martensite. Mater. Sci. Eng. A. https://doi.org/10.1016/j.msea.2014.05.078

He, D., Zhu, J., Zaefferer, S., Raabe, D., 2014. Effect of retained beta layer on slip transmission in Ti-6Al-2Zr-1Mo-1V near alpha titanium alloy during tensile deformation at room temperature. Mater. Des. https://doi.org/10.1016/j.matdes.2013.12.018

Hémery, S., Naït-Ali, A., Guéguen, M., Wendorf, J., Polonsky, A.T., Echlin, M.P., Stinville, J.C., Pollock, T.M., Villechaise, P., 2019. A 3D analysis of the onset of slip activity in relation to the degree of micro-texture in Ti–6Al–4V. Acta Mater. https://doi.org/10.1016/j.actamat.2019.09.028

Hémery, S., Nizou, P., Villechaise, P., 2018. In situ SEM investigation of slip transfer in Ti-6Al-4V: Effect of applied stress. Mater. Sci. Eng. A. https://doi.org/10.1016/j.msea.2017.10.058

Hémery, S., Villechaise, P., Banerjee, D., 2020. Microplasticity at Room Temperature in α/β Titanium Alloys. Metall. Mater. Trans. A 1. https://doi.org/10.1007/s11661-020-05945-4

Hoefnagels, J.P.M., Tasan, C.C., Maresca, F., Peters, F.J., Kouznetsova, V.G., 2015. Retardation of plastic instability via damage-enabled microstrain delocalization. J. Mater. Sci. https://doi.org/10.1007/s10853-015-9164-0

Johnson, G.R., Cook, W.H., 1985. Fracture characteristics of three metals subjected to various strains, strain rates, temperatures and pressures. Eng. Fract. Mech. https://doi.org/10.1016/0013-7944(85)90052-9

Joseph, S., Lindley, T.C., Dye, D., 2018. Dislocation interactions and crack nucleation in a fatigued near-Alpha titanium alloy. Int. J. Plast. https://doi.org/10.1016/j.ijplas.2018.06.009

Jun, T.S., Maeder, X., Bhowmik, A., Guillonneau, G., Michler, J., Giuliani, F., Britton, T. Ben, 2019. The role of β-titanium ligaments in the deformation of dual phase titanium alloys. Mater. Sci. Eng. A. https://doi.org/10.1016/j.msea.2019.01.032

Kapoor, K., Yoo, Y.S.J., Book, T.A., Kacher, J.P., Sangid, M.D., 2018. Incorporating grain-level residual stresses and validating a crystal plasticity model of a two-phase Ti-6Al-4 V alloy produced via additive manufacturing. J. Mech. Phys. Solids. https://doi.org/10.1016/j.jmps.2018.07.025

Kasemer, M., Echlin, M.P., Stinville, J.C., Pollock, T.M., Dawson, P., 2017. On slip initiation in equiaxed α/β Ti-6Al-4V. Acta Mater. 136, 288–302. https://doi.org/10.1016/j.actamat.2017.06.059

Khosravani, A., Cecen, A., Kalidindi, S.R., 2017. Development of high throughput assays for establishing process-structure-property linkages in multiphase polycrystalline metals: Application to dual-phase steels. Acta Mater. https://doi.org/10.1016/j.actamat.2016.10.033

Kim, J.H., Semiatin, S.L., Lee, C.S., 2008. High-temperature deformation and grain-boundary characteristics of titanium alloys with an equiaxed microstructure. Mater. Sci. Eng. A. https://doi.org/10.1016/j.msea.2007.08.027

Kuang, S., Kang, Y. lin, Yu, H., Liu, R. dong, 2009. Stress-strain partitioning analysis of constituent phases in dual phase steel based on the modified law of mixture. Int. J. Miner. Metall. Mater. https://doi.org/10.1016/S1674-4799(09)60070-4

Lai, Q., Bouaziz, O., Gouné, M., Brassart, L., Verdier, M., Parry, G., Perlade, A., Bréchet, Y., Pardoen, T., 2015. Damage and fracture of dual-phase steels: Influence of martensite volume fraction. Mater. Sci. Eng. A. https://doi.org/10.1016/j.msea.2015.08.073

Latypov, M.I., Shin, S., De Cooman, B.C., Kim, H.S., 2016. Micromechanical finite element analysis of strain partitioning in multiphase medium manganese TWIP+TRIP steel. Acta Mater. 108, 219–228. https://doi.org/10.1016/j.actamat.2016.02.001

Lefranc, P., Doquet, V., Gerland, M., Sarrazin-Baudoux, C., 2008. Nucleation of cracks from shear-induced cavities in an α/β titanium alloy in fatigue, room-temperature creep and dwell-fatigue. Acta Mater. https://doi.org/10.1016/j.actamat.2008.04.060

Li, M., Duquette, D.J., Chen, Y., 2019. Deformation Accommodation at Triple Junctions in Columnar-Grained Nickel. Metall. Mater. Trans. A Phys. Metall. Mater. Sci. https://doi.org/10.1007/s11661-018-4998-0

Luster, J., Morris, M.A., 1995. Compatibility of deformation in two-phase Ti-Al alloys: Dependence on microstructure and orientation relationships. Metall. Mater. Trans. A. https://doi.org/10.1007/BF02670762

Ma, C., Wang, H., Hama, T., Guo, X., Mao, X., Wang, J., Wu, P., 2019. Twinning and detwinning behaviors of commercially pure titanium sheets. Int. J. Plast. https://doi.org/10.1016/j.ijplas.2019.06.010

Maraghechi, S., Hoefnagels, J.P.M., Peerlings, R.H.J., Rokoš, O., Geers, M.G.D., 2019. Correction of Scanning Electron Microscope Imaging Artifacts in a Novel Digital Image Correlation Framework. Exp. Mech. https://doi.org/10.1007/s11340-018-00469-w

Matsuno, T., Teodosiu, C., Maeda, D., Uenishi, A., 2015. Mesoscale simulation of the early evolution of ductile fracture in dual-phase steels. Int. J. Plast. https://doi.org/10.1016/j.ijplas.2015.06.004

Mazaheri, Y., Kermanpur, A., Najafizadeh, A., 2015. Nanoindentation study of ferrite-martensite dual phase steels developed by a new thermomechanical processing. Mater. Sci. Eng. A. https://doi.org/10.1016/j.msea.2015.04.098

McClintock, F.A., 1964. A criterion for ductile fracture by the growth of holes. J. Appl. Mech. Trans. ASME. https://doi.org/10.1115/1.3601204

McMurtrey, M.D., Was, G.S., Cui, B., Robertson, I., Smith, L., Farkas, D., 2014. Strain localization at dislocation channel-grain boundary intersections in irradiated stainless steel. Int. J. Plast. https://doi.org/10.1016/j.ijplas.2014.01.001

Min, X.H., Zhang, L., Sekido, K., Ohmura, T., Emura, S., Tsuchiya, K., Tsuzaki, K., 2012. Strength evaluation of α and β phases by nanoindentation in Ti-15Mo alloys with Fe and Al addition. Mater. Sci. Technol. https://doi.org/10.1179/1743284711Y.0000000052

Morsdorf, L., Tasan, C.C., Ponge, D., Raabe, D., 2015. 3D structural and atomic-scale analysis of lath martensite: Effect of the transformation sequence. Acta Mater. https://doi.org/10.1016/j.actamat.2015.05.023

Musinski, W.D., McDowell, D.L., 2016. Simulating the effect of grain boundaries on microstructurally small fatigue crack growth from a focused ion beam notch through a three-dimensional array of grains. Acta Mater. https://doi.org/10.1016/j.actamat.2016.04.006

Nayak, S.K., Hung, C.J., Sharma, V., Alpay, S.P., Dongare, A.M., Brindley, W.J., Hebert, R.J., 2018. Insight into point defects and impurities in titanium from first principles. npj Comput. Mater. https://doi.org/10.1038/s41524-018-0068-9

Nervo, L., King, A., Fitzner, A., Ludwig, W., Preuss, M., 2016. A study of deformation twinning in a titanium alloy by X-ray diffraction contrast tomography. Acta Mater. https://doi.org/10.1016/j.actamat.2015.12.032

Ososkov, Y., Wilkinson, D.S., Jain, M., Simpson, T., 2007. In-situ measurement of local strain partitioning in a commercial dual-phase steel. Zeitschrift fuer Met. Res. Adv. Tech. https://doi.org/10.3139/146.101526

Peters, M., Leyens, C., 2003. Titanium and Titanium Alloys: Fundamentals and Applications, Titanium and Titanium Alloys Fundamentals and Applications. https://doi.org/10.1002/3527602119

Pharr, G.M., Bolshakov, A., 2002. Understanding nanoindentation unloading curves. J. Mater. Res. https://doi.org/10.1557/JMR.2002.0386

Proust, G., Tomé, C.N., Kaschner, G.C., 2007. Modeling texture, twinning and hardening evolution during deformation of hexagonal materials. Acta Mater. https://doi.org/10.1016/j.actamat.2006.11.017

Pütz, F., Shen, F., Könemann, M., Münstermann, S., 2020. The differences of damage initiation and accumulation of DP steels: a numerical and experimental analysis. Int. J. Fract. https://doi.org/10.1007/s10704-020-00457-z

Roters, F., Eisenlohr, P., Bieler, T.R., Raabe, D., 2010. Crystal Plasticity Finite Element Methods, Crystal Plasticity Finite Element Methods. https://doi.org/10.1002/9783527631483

Rui, S.-S., Niu, L.-S., Shi, H.-J., Wei, S., Tasan, C.C., 2019. Diffraction-based misorientation mapping: A continuum mechanics description. J. Mech. Phys. Solids 133, 103709. https://doi.org/10.1016/j.jmps.2019.103709

Ryu, J.H., Kim, D.I., Kim, H.S., Bhadeshia, H.K.D.H., Suh, D.W., 2010. Strain partitioning and mechanical stability of retained austenite. Scr. Mater. 63, 297–299. https://doi.org/10.1016/j.scriptamat.2010.04.020

Savage, M.F., Tatalovich, J., Mills, M.J., 2004. Anisotropy in the room-temperature deformation of α-β colonies in titanium alloys: Role of the α-β interface. Philos. Mag. https://doi.org/10.1080/14786430320001583 05

Scholz, F., 1997. Interfaces in crystalline materials (1996) A. P. Sutton, R. W. Balluffi. J. Solid State Electrochem. https://doi.org/10.1007/s100080050033

Seal, J.R., Crimp, M.A., Bieler, T.R., Boehlert, C.J., 2012. Analysis of slip transfer and deformation behavior across the α/β interface in Ti-5Al-2.5Sn (wt.%) with an equiaxed microstructure. Mater. Sci. Eng. A. https://doi.org/10.1016/j.msea.2012.04.114

Semiatin, S.L., 2020. An Overview of the Thermomechanical Processing of α/β Titanium Alloys: Current Status and Future Research Opportunities. Metall. Mater. Trans. A Phys. Metall. Mater. Sci. https://doi.org/10.1007/s11661-020-05625-3

Shao, H., Zhao, Y., Ge, P., Zeng, W., 2013. Crack initiation and mechanical properties of TC21 titanium alloy with equiaxed

microstructure. Mater. Sci. Eng. A. https://doi.org/10.1016/j.msea.2013.08.012

Sperry, R., Harte, A., Quinta da Fonseca, J., Homer, E.R., Wagoner, R.H., Fullwood, D.T., 2020. Slip band characteristics in the presence of grain boundaries in nickel-based superalloy. Acta Mater. https://doi.org/10.1016/j.actamat.2020.04.037

Stapleton, A.M., Raghunathan, S.L., Bantounas, I., Stone, H.J., Lindley, T.C., Dye, D., 2008. Evolution of lattice strain in Ti-6Al-4V during tensile loading at room temperature. Acta Mater. https://doi.org/10.1016/j.actamat.2008.08.030

Stinville, J.C., Echlin, M.P., Texier, D., Bridier, F., Bocher, P., Pollock, T.M., 2016. Sub-Grain Scale Digital Image Correlation by Electron Microscopy for Polycrystalline Materials during Elastic and Plastic Deformation. Exp. Mech. 56, 197–216. https://doi.org/10.1007/s11340-015-0083-4

Stinville, J.C., Francis, T., Polonsky, A.T., Torbet, C.J., Charpagne, M.A., Chen, Z., Balbus, G.H., Bourdin, F., Valle, V., Callahan, P.G., Echlin, M.P., Pollock, T.M., 2021. Time-Resolved Digital Image Correlation in the Scanning Electron Microscope for Analysis of Time-Dependent Mechanisms. Exp. Mech. 61, 331–348. https://doi.org/10.1007/s11340-020-00632-2

Sun, J., Jin, L., Dong, J., Wang, F., Dong, S., Ding, W., Luo, A.A., 2019. Towards high ductility in magnesium alloys - The role of intergranular deformation. Int. J. Plast. https://doi.org/10.1016/j.ijplas.2019.07.014

Suri, S., Viswanathan, G.B., Neeraj, T., Hou, D.H., Mills, M.J., 1999. Room temperature deformation and mechanisms of slip transmission in oriented single-colony crystals of an α/β titanium alloy. Acta Mater. https://doi.org/10.1016/S1359-6454(98)00364-4

Sutton, M.A., Hild, F., 2015. Recent Advances and Perspectives in Digital Image Correlation. Exp. Mech. https://doi.org/10.1007/s11340-015-9991-6

Takahashi, A., Seko, A., Tanaka, I., 2017. Conceptual and practical bases for the high accuracy of machine learning interatomic potentials: Application to elemental titanium. Phys. Rev. Mater. https://doi.org/10.1103/PhysRevMaterials.1.063801

Tang, A., Liu, H., Liu, G., Zhong, Y., Wang, L., Lu, Q., Wang, J., Shen, Y., 2020. Lognormal Distribution of Local Strain: A Universal Law of Plastic Deformation in Material. Phys. Rev. Lett. https://doi.org/10.1103/PhysRevLett.124.155501

Tasan, C.C., Diehl, M., Yan, D., Bechtold, M., Roters, F., Schemmann, L., Zheng, C., Peranio, N., Ponge, D., Koyama, M., Tsuzaki, K., Raabe, D., 2015. An Overview of Dual-Phase Steels: Advances in Microstructure-Oriented Processing and Micromechanically Guided Design. Annu. Rev. Mater. Res. https://doi.org/10.1146/annurev-matsci-070214-021103

Tasan, C.C., Diehl, M., Yan, D., Zambaldi, C., Shanthraj, P., Roters, F., Raabe, D., 2014a. Integrated experimental-simulation analysis of stress and strain partitioning in multiphase alloys. Acta Mater. https://doi.org/10.1016/j.actamat.2014.07.071

Tasan, C.C., Hoefnagels, J.P.M., Diehl, M., Yan, D., Roters, F., Raabe, D., 2014b. Strain localization and damage in dual phase steels investigated by coupled in-situ deformation experiments and crystal plasticity simulations. Int. J. Plast. https://doi.org/10.1016/j.ijplas.2014.06.004

Taylor, M.D., Choi, K.S., Sun, X., Matlock, D.K., Packard, C.E., Xu, L., Barlat, F., 2014. Correlations between nanoindentation hardness and macroscopic mechanical properties in DP980 steels. Mater. Sci. Eng. A. https://doi.org/10.1016/j.msea.2013.12.084

Toby, B.H., Von Dreele, R.B., 2013. GSAS-II: The genesis of a modern open-source all purpose crystallography software package. J. Appl. Crystallogr. https://doi.org/10.1107/S0021889813003531

Toda, H., Takijiri, A., Azuma, M., Yabu, S., Hayashi, K., Seo, D., Kobayashi, M., Hirayama, K., Takeuchi, A., Uesugi, K., 2017. Damage micromechanisms in dual-phase steel investigated with combined phase- and absorption-contrast tomography. Acta Mater. https://doi.org/10.1016/j.actamat.2017.01.010

Venkatramani, G., Ghosh, S., Mills, M., 2007. A size-dependent crystal plasticity finite-element model for creep and load shedding in polycrystalline titanium alloys. Acta Mater. https://doi.org/10.1016/j.actamat.2007.03.017

W.C. Oliver; G.M. Phar, 1992. An improved technique for determining hardness and elastic modulus using load and displacement sensing indentation experiments. J. Mater. Res. 7, p 1564-1583. https://doi.org/10.1557/JMR.1992.1564

Waheed, S., Zheng, Z., Balint, D.S., Dunne, F.P.E., 2019. Microstructural effects on strain rate and dwell sensitivity in dual-phase titanium alloys. Acta Mater. https://doi.org/10.1016/j.actamat.2018.09.035

Wang, K., Yan, Z., Zhou, Y., Wei, S., Wang, X., Xin, R., Liu, Q., 2020. Slip initiation in interlayered β and corresponding slip transfer during compression of a lamellar-structure titanium alloy. Results Phys. https://doi.org/10.1016/j.rinp.2020.103276

Wang, L., Yang, Y., Eisenlohr, P., Bieler, T.R., Crimp, M.A., Mason, D.E., 2010. Twin nucleation by slip transfer across grain boundaries in commercial purity titanium. Metall. Mater. Trans. A Phys. Metall. Mater. Sci. https://doi.org/10.1007/s11661-009-0097-6

Wang, M.M., Hell, J.C., Tasan, C.C., 2017. Martensite size effects on damage in quenching and partitioning steels. Scr. Mater. https://doi.org/10.1016/j.scriptamat.2017.05.021

Warwick, J.L.W., Coakley, J., Raghunathan, S.L., Talling, R.J., Dye, D., 2012a. Effect of texture on load partitioning in Ti-6Al-4V. Acta Mater. https://doi.org/10.1016/j.actamat.2012.03.039

Warwick, J.L.W., Jones, N.G., Rahman, K.M., Dye, D., 2012b. Lattice strain evolution during tensile and compressive loading of CP Ti. Acta Mater. https://doi.org/10.1016/j.actamat.2012.08.042

Wei, S., Huang, L., Li, X., Jiao, Y., Ren, W., Geng, L., 2019a. Network-Strengthened Ti-6Al-4V/(TiC+TiB) Composites: Powder Metallurgy Processing and Enhanced Tensile Properties at Elevated Temperatures. Metall. Mater. Trans. A 50, 3629–3645. https://doi.org/10.1007/s11661-019-05244-7

Wei, S., Kim, J., Cann, J.L., Gholizadeh, R., Tsuji, N., Tasan, C.C., 2020. Plastic strain-induced sequential martensitic transformation. Scr. Mater. 185, 36–41. https://doi.org/10.1016/j.scriptamat.2020.03.060

Wei, S., Kim, J., Tasan, C.C., 2019b. Boundary micro-cracking in metastable Fe 45 Mn 35 Co 10 Cr 10 high-entropy alloys. Acta Mater. 168, 76–86. https://doi.org/10.1016/j.actamat.2019.01.036

Wei, S., Zhu, G., Tasan, C.C., 2021. Slip-twinning interdependent activation across phase boundaries: An in-situ investigation of a Ti-Al-V-Fe (α+β) alloy. Acta Mater. https://doi.org/10.1016/j.actamat.2020.116520

Wei, S.L., Huang, L.J., Chang, J., Zhai, W., Yang, S.J., Geng, L., 2016. Primary phase growth and microstructure evolution of rapidly solidifying ternary Ti-12Al-8V alloy. Mater. Lett. 175, 291–295. https://doi.org/10.1016/j.matlet.2016.04.043

Wood, R.M., 1962. The lattice constants of high purity alpha titanium. Proc. Phys. Soc. https://doi.org/10.1088/0370-1328/80/3/323

Wu, H., Fan, G., 2020. An overview of tailoring strain delocalization for strength-ductility synergy. Prog. Mater. Sci. https://doi.org/10.1016/j.pmatsci.2020.100675

Wu, H., Huang, M., Li, X., Xia, Y., Wang, Z., Fan, G., 2021. Temperature-dependent reversed fracture behavior of multilayered TiBw/Ti-Ti(Al) composites. Int. J. Plast. https://doi.org/10.1016/j.ijplas.2021.102998

Xu, Y., Dan, W., Li, C., Zhang, W., 2020. Experimental Study of the Micromechanical Behavior of Ferrite in DP Steel Under Various Stress States. Metall. Mater. Trans. A Phys. Metall. Mater. Sci. https://doi.org/10.1007/s11661-020-05867-1

Xu, Y., Joseph, S., Karamched, P., Fox, K., Rugg, D., Dunne, F.P.E., Dye, D., 2020. Predicting dwell fatigue life in titanium alloys using modelling and experiment. Nat. Commun. https://doi.org/10.1038/s41467-020-19470-w

Yan, D., Tasan, C.C., Raabe, D., 2015. High resolution in situ mapping of microstrain and microstructure evolution reveals damage resistance criteria in dual phase steels. Acta Mater. 96, 399–409. https://doi.org/10.1016/j.actamat.2015.05.038

Yang, Y., Wang, L., Bieler, T.R., Eisenlohr, P., Crimp, M.A., 2011. Quantitative atomic force microscopy characterization and crystal plasticity finite element modeling of heterogeneous deformation in commercial purity titanium, in: Metallurgical and Materials Transactions A: Physical Metallurgy and Materials Science. https://doi.org/10.1007/s11661-010-0475-0

Yoo, M.H., 1981. Slip, twinning, and fracture in hexagonal close-packed metals. Metall. Trans. A. https://doi.org/10.1007/BF02648537

Young, R.A., Prince, E., Sparks, R.A., 1982. Suggested guidelines for the publication of Rietveld analyses and pattern decomposition studies. J. Appl. Crystallogr. https://doi.org/10.1107/s0021889882012138

Yu, T., Du, Y., Fan, G., Xu, R., Barabash, R., Hansen, N., Huang, X., Zhang, Y., 2021. In-situ synchrotron X-ray micro-diffraction investigation of ultra-low-strain deformation microstructure in laminated Ti-Al composites. Acta Mater. https://doi.org/10.1016/j.actamat.2020.10.050

Zhang, X., Zhang, S., Zhao, Q., Zhao, Y., Li, R., Zeng, W., 2018. In-situ observations of the tensile deformation and fracture behavior of a fine-grained titanium alloy sheet. J. Alloys Compd. https://doi.org/10.1016/j.jallcom.2018.01.009

Zhang, Z., Jun, T.S., Britton, T.B., Dunne, F.P.E., 2016. Determination of Ti-6242 α and β slip properties using micro-pillar test and computational crystal plasticity. J. Mech. Phys. Solids. https://doi.org/10.1016/j.jmps.2016.06.007

Zhang, Z., Lunt, D., Abdolvand, H., Wilkinson, A.J., Preuss, M., Dunne, F.P.E., 2018. Quantitative investigation of micro slip and localization in polycrystalline materials under uniaxial tension. Int. J. Plast. https://doi.org/10.1016/j.ijplas.2018.04.014

Zhao, P., Shen, C., Savage, M.F., Li, J., Niezgoda, S.R., Mills, M.J., Wang, Y., 2019. Slip transmission assisted by Shockley partials across α/β interfaces in Ti-alloys. Acta Mater. https://doi.org/10.1016/j.actamat.2019.04.013

Zheng, Z., Balint, D.S., Dunne, F.P.E., 2017a. Mechanistic basis of temperature-dependent dwell fatigue in titanium alloys. J. Mech. Phys. Solids. https://doi.org/10.1016/j.jmps.2017.07.010

Zheng, Z., Balint, D.S., Dunne, F.P.E., 2017b. Investigation of slip transfer across HCP grain boundaries with application to cold dwell facet fatigue. Acta Mater. https://doi.org/10.1016/j.actamat.2017.01.021

Zheng, Z., Waheed, S., Balint, D.S., Dunne, F.P.E., 2018. Slip transfer across phase boundaries in dual phase titanium alloys and the effect on strain rate sensitivity. Int. J. Plast. https://doi.org/10.1016/j.ijplas.2018.01.011

Zhou, P., Xu, S., Xiao, D., Jiang, C., Hu, Y., Wang, J., 2019. Shock-induced {1121}→{1122} double twinning in titanium. Int. J. Plast. https://doi.org/10.1016/j.ijplas.2018.08.014